

# Exo-Zodiacal Dust Levels for Nearby Main-Sequence Stars: A Survey with the Keck Interferometer Nuller

R. Millan-Gabet

California Institute of Technology, NASA Exoplanet Science Institute, Pasadena, CA  
91125, USA

R.Millan-Gabet@caltech.edu

E. Serabyn, B. Mennesson, W. A. Traub

Jet Propulsion Laboratory, California Institute of Technology, 4800 Oak Grove Drive,  
Pasadena, CA 91109, USA

R. K. Barry, W. C. Danchi, M. Kuchner

NASA Goddard Space Flight Center, Exoplanets and Stellar Astrophysics Laboratory,  
Code 667, Greenbelt, MD 20771, USA

S. Ragland, M. Hrynevych, J. Woillez

Keck Observatory, 65-1120 Mamalahoa Hwy, Kamuela, HI 96743, USA

and

K. Stapelfeldt, G. Bryden, M. M. Colavita, A. J. Booth

Jet Propulsion Laboratory, California Institute of Technology, 4800 Oak Grove Drive,  
Pasadena, CA 91109, USA

Received \_\_\_\_\_; accepted \_\_\_\_\_

Accepted by ApJ April 7 2011

**ABSTRACT**

The Keck Interferometer Nuller (KIN) was used to survey 25 nearby main sequence stars in the mid-infrared, in order to assess the prevalence of warm circumstellar (exozodiacal) dust around nearby solar-type stars. The KIN measures circumstellar emission by spatially blocking the star but transmitting the circumstellar flux in a region typically 0.1 – 4 AU from the star. We find one significant detection ( $\eta$  Crv), two marginal detections ( $\gamma$  Oph and  $\alpha$  Aql), and 22 clear non-detections. Using a model of our own Solar System’s zodiacal cloud, scaled to the luminosity of each target star, we estimate the equivalent number of target zodi needed to match our observations. Our three zodi detections are  $\eta$  Crv ( $1250 \pm 260$ ),  $\gamma$  Oph ( $200 \pm 80$ ) and  $\alpha$  Aql ( $600 \pm 200$ ), where the uncertainties are  $1\sigma$ . The 22 non-detected targets have an ensemble weighted average consistent with zero, with an average individual uncertainty of 160 zodi ( $1\sigma$ ). These measurements represent the best limits to date on exozodi levels for a sample of nearby main sequence stars. A statistical analysis of the population of 23 stars not previously known to contain circumstellar dust (excluding  $\eta$  Crv and  $\gamma$  Oph) suggests that, if the measurement errors are uncorrelated (for which we provide evidence) and if these 23 stars are representative of a single class with respect to the level of exozodi brightness, the mean exozodi level for the class is  $< 150$  zodi ( $3\sigma$  upper-limit, corresponding to 99% confidence under the additional assumption that the measurement errors are Gaussian). We also demonstrate that this conclusion is largely independent of the shape and mean level of the (unknown) true underlying exozodi distribution.

*Subject headings:* techniques: high angular resolution — planetary systems: zodiacal dust — stars: circumstellar matter

## 1. Introduction

The present day Solar System contains interplanetary dust. The term *zodiacal* usually refers to the dust present in the inner Solar System, out to  $\sim 5$  AU. It currently has a fractional luminosity of  $L_{dust}/L_{\odot} \sim 10^{-7}$  (Backman & Paresce 1993) and  $10^{-10}$  the mass of the planets, but an infrared luminosity  $100\times$  larger. Because the survival times for small particles in the radiation and wind environment of the star is a few 100 to a few 1000 yrs, any such circumstellar dust observed in stars older than a few tens of millions of years must be recently formed and continuously generated. The presence of prominent dust bands in the solar zodiacal cloud associated with asteroid families suggest that the zodiacal cloud arises from the breakup of main belt asteroids (see e.g. Dermott et al. 1984). However, recent models of zodiacal dust production imply that the splitting of short period comets could be the dominant source (Nesvorný et al. 2010).

Circumstellar dust around other mature stars was originally discovered, unexpectedly, by IRAS (Aumann et al. (1984), see e.g. the review by Backman & Paresce (1993)), and has since been observationally studied by a variety of ground and space observatories, via both their thermal and scattered emission. Most commonly, the phenomenon reveals itself as long-wavelength fluxes in excess of what is expected from the stellar photosphere alone, but spatially resolved images of the outer disk regions have also been obtained for a few of the most extreme systems (see e.g. the review by Zuckerman 2001). The term *debris* disk usually refers to the entire dust distribution, extending to 100s of astronomical units (AU) from the Sun.

The presence of high levels of cold outer dust around main sequence stars is now known to be a ubiquitous phenomenon (e.g. 30% of all A-stars, and 13% of solar-type stars Rieke et al. 2005; Su et al. 2006; Bryden et al. 2006; Beichman et al. 2006b). However, very few stars have had positive detections of excess flux at wavelengths  $< 30\mu\text{m}$  (Beichman

et al. 2006a; Lawler et al. 2009). Although this rarity appears to be consistent with evolution models and detection thresholds, the fact remains that much less is known about levels of inner warm dust, of most interest to extra-solar terrestrial planets searches. The measurement is difficult, because the dust emission is close to and faint compared to the parent star. Thus, we currently have no firm estimates of the warm zodi brightness around nearby stars, or around any stars. Interestingly, the few systems that have been imaged in some detail at sub-mm wavelengths display a striking variety of complex morphological features. This forces caution when interpreting spatially unresolved observations, and highlights the difficulties in attempting to infer levels of inner warm dust from measurements made at wavelengths which probe very different spatial scales.

Searches for exozodiacal emission from warm inner dust have been attempted from the ground (e.g. Kuchner et al. 1998; Liu et al. 2004) and space (e.g. Beichman et al. 2006a; Lawler et al. 2009). Due to current limitations of the observational techniques, known exozodi disks have much higher dust densities than the Solar System (e.g.  $L_{dust}/L_{\star} > 10^{-4}$  from the Lawler et al. (2009) survey); the present-day Solar System zodiacal levels would be currently undetectable around other stars.

Studying exozodi clouds is of interest for a variety of reasons. Among them, the time-scales for debris disk evolution may help understand terrestrial planet formation (see e.g. Wyatt 2008), and disk structure may be used to infer the presence of perturbing unseen exo-planets (Wolf et al. 2007; Stark & Kuchner 2008), examples of which have now been directly imaged (Marois et al. 2008; Kalas et al. 2008). Moreover, both the levels of exozodi emission and their spatial structure act as sources of noise that may hinder the direct detection and characterization of terrestrial exoplanets by spaced-based coronagraphic or interferometric techniques (e.g. Beckwith 2008). Indeed the largest uncertainty in estimating planet detection efficiencies is due to exozodi dust. Since exozodi photons impact

the required integration times and sample sizes for a given mission lifetime, knowledge of exozodi levels and structure for all candidate stars would allow a greatly optimized instrument and observing strategy design.

Mid-infrared interferometry has provided exozodi measurements at high spatial resolution for specific known high-dust stars (Stark et al. 2009; Smith et al. 2009). Interferometric techniques have also enabled the identification of an intriguing source of near-infrared excess around some main sequence stars (Absil et al. 2008, 2006; Akeson et al. 2009; Absil et al. 2009). Obtaining exozodi measurements for relatively large samples of representative nearby main sequence stars was the primary scientific driver for the development of the Keck Interferometer Nuller (KIN), and for the execution of a 1-year long intensive Key Science observing campaign shared among three selected proposals. This paper summarizes the results from one of three Key Science programs selected (“The Keck Interferometer Nuller Survey of Exozodiacal Dust around Nearby Stars”, Principal Investigator: G. Serabyn).

## 2. The Sample

Of all nearby stars,  $\sim 85$  dwarfs and sub-dwarfs fall within the sensitivity and observability limits of the KIN. Given the expected time allocation for the Key Science programs, we down-selected this list to 40 high priority objects, containing systems both with and without known debris disk emission (a.k.a “high dust” and “low dust”, respectively) as inferred from mid-infrared spectrophotometric measurements. The selecting committee ultimately assigned 5 high dust and 24 low dust objects to the program described here. Of those, 25 systems were actually observed, 2 high dust ( $\eta$  Crv and  $\gamma$  Oph) and 23 low dust. Observations took place in service mode during the period February 2008 – January 2009, over 32 nights shared with the other two Key Science programs. Table 1

describes our list of observed targets, including all the brightnesses relevant to the various KIN subsystems, and the stellar parameters relevant to our modeling approach.

### 3. The Keck Interferometer Nuller

#### 3.1. Instrument Overview

The Keck Interferometer Nuller (Colavita et al. 2009) operates in N-band ( $8.0\text{--}13.0\mu\text{m}$ ) and combines the light from the two Keck telescopes as an interferometer with a physical baseline length  $B \sim 85$  m. The KIN produces a dark fringe through the phase center (“Nulling”). The adjacent bright fringe (through which flux is transmitted), projects onto the sky at an angular separation  $\lambda/2B = 10$  mas, or 0.1 AU at the median distance to the stars in our sample (10.5 pc), and for  $\lambda = 8.5\mu\text{m}$  (the effective wavelength of the KIN bandpass). Thus, the instrument is sensitive to circumstellar dust located as close to the central star as these spatial scales (i.e. “inner working angle”). Blackbody emission peaks at  $8.5\mu\text{m}$  for  $T \sim 432$  K. For the median luminosity of the stars in our sample ( $2.2L_{\odot}$ ), dust particles in thermal equilibrium at this temperature are located at a stellocentric radius of 0.3 AU. Therefore, the KIN fringe spacing matches well the expected location of relatively warm dust, located in the inner disk regions. The KIN can observe objects as faint as  $N(\text{flux}) = 1.7$  Jy, as long as they also have  $K_{\text{mag}} < 6$  (K-band co-phasing limit) and  $J_{\text{mag}} < 8.5$  (angle tracking limit).<sup>1</sup>

The response of any interferometer may be understood by projecting the fringe pattern on the sky: what is measured is the astrophysical flux from the surface brightness transmitted through the fringe pattern. For the work presented here, we measure and

---

<sup>1</sup>see <http://nexsci.caltech.edu/software/KISupport/nulling/> for a full description of the instrument parameters.

calibrate the transmitted flux (expected to be small) due to dust surrounding the central target stars. Thus, we refer to the basic observable as the “flux leakage” or simply the “leak” (the inverse quantity, the null depth, is an equivalent and also frequently used term, i.e. leak = 0.01 implies null depth 100:1). The amount of flux leakage not attributable to the finite size of the central stars is referred to as “excess leakage”, and by measuring it we can learn about the amounts of circumstellar dust present.

In order to achieve good accuracy of the calibrated leak measurements, the KIN utilizes an architecture in which each Keck pupil is split into two halves, resulting in two Keck–Keck long baselines, and two short baselines (4 m) formed between the two halves of each Keck telescope. In order to accommodate the large dynamic range between a star and any surrounding dust, the star is nulled on the Keck–Keck baselines. In order to detect small leakage signals in the presence of the large mid–infrared background, the nulled outputs are combined on the short baselines in a standard Michelson combiner (a.k.a. the “cross–combiner”, or XC) with fast optical path difference modulation (i.e. “interferometric chopping”, see also Mennesson et al. 2005). The output of the short baseline combiners (for which any object appears essentially unresolved) when the long baselines are “at peak” also provide the necessary flux normalization of the leak measurement. In essence then, the KIN measurement is the ratio of the amplitudes of the short baseline combiner fringes when the long baseline combiner is set at null, divided by the same quantity when the long baseline combiner is set at peak:

$$L_{raw} = \frac{\text{XC fringe amplitude at null}}{\text{XC fringe amplitude at peak}} \quad (1)$$

The many details involved in making this measurement are described in Colavita et al. (2009) and Colavita et al. (2010). As emphasized in those references, in a ground–based background limited environment, achieving a high level of suppression of the central star

(i.e. deep nulls) is not the most important consideration. Equally important is being able to calibrate the leaks well; and the KIN four-beam architecture results in a better calibration of the measured leakages (or equivalent visibilities) compared to standard Michelson interferometry at mid-infrared wavelengths.

Due to various instrumental factors (diffraction, material absorption, pinhole mode matching), the KIN spectral responsivity is strongly peaked toward the blue end of the bandpass; the  $8 - 9\mu\text{m}$  bin contains most of the signal-to-noise ratio (SNR). Also, the red end of the spectrum is affected by poorer calibration quality (believed to be caused by residual correlation in the short baseline combiners arising from telescope thermal emission). Thus, for the analysis presented here, we only use the  $8 - 9\mu\text{m}$  spectral bin, most sensitive to exozodi detection.

### 3.2. Sky Response

As noted above, the KIN response may be understood as the flux from the astrophysical source that is transmitted through its fringe pattern projected on the sky. Due to its four-beam architecture, the KIN beam pattern consists of three terms:

1. Point spread function (PSF) of each Keck half-aperture ( $T_{PSF}$ ); this is well approximated at  $8.5\mu\text{m}$  by an elliptical Gaussian of  $\text{FWHM} = 490 \times 440$  mas. For the observations presented here, the Keck rotator angles are oriented such that this pattern has the major-axis along the East-West direction, and rotates as the target moves across the sky such that the minor-axis always points toward North.
2. Fringes of the short baseline combiner ( $T_{XC}$ ):

$$T_{XC} = \cos(2\pi(x \cdot u_{xc} + y \cdot v_{xc})) \tag{2}$$



where  $(x, y)$  are coordinate offsets in right ascension and declination, and  $(u_{xc}, v_{xc})$  are the corresponding short baseline spatial frequencies. These fringes are perpendicular to the half-pupil PSF major-axis, and rotate in the same way. Projected on the sky, this fringe pattern is relatively “broad”: at  $8.5 \mu\text{m}$  the fringe spacing for the physical 4 m short baseline is 440 mas.

3. Fringes of the long baseline combiner ( $T_{long}$ ):

$$T_{long} = \frac{1}{2} \cdot (1 \mp \cos(2\pi(x \cdot u + y \cdot v))) \quad (3)$$

where  $(u, v)$  are the long baseline spatial frequencies, and the  $\mp$  corresponds to the null/peak configuration, respectively. This fringe pattern can have any orientation with respect to  $T_{PSF}$  and  $T_{XC}$ . As mentioned above, in this “fine” fringe pattern the dark and bright fringes are spaced by an angular separation projected on the sky of 10 mas, at  $8.5 \mu\text{m}$  and for the physical 85 m KI baseline.

The total KIN transmission pattern is thus:

$$T(x, y, u, v, u_{xc}, v_{xc}, \lambda) = T_{PSF} \cdot T_{XC} \cdot T_{long} \quad (4)$$

Through the dependence on the spatial frequencies, the instantaneous KIN pattern depends on wavelength ( $8.5 \mu\text{m}$ ) and on the hour angle and declination of the target being observed. Figure 1 shows an example of the KIN pattern terms. The KIN is sensitive to circumstellar dust by its ability to measure its flux transmitted through the total KIN fringe pattern (center panel of Figure 1) i.e. dust located from  $\sim 10$  mas (0.1 AU at 10 pc) out to the  $\sim 490 \times 440$  mas field-of-view. However, the short baseline fringes ( $T_{XC}$ ) also act to limit the KIN’s ability to detect outer dust. Indeed, in the example shown in Figure 1

(top-right panel),  $T_{XC}$  goes to zero at  $\sim 110$  mas along the small baseline direction, so that the “effective FOV” is only  $\sim 110 \times 440$  mas ( $\sim 1.1 \times 4.4$  AU at 10 pc).

For an object with a brightness distribution  $I(x, y, \lambda)$ , the expected monochromatic leak is thus:

$$L_{calculated}(u, v, u_{xc}, v_{xc}, \lambda) = \frac{\int \int I(x, y, \lambda) \cdot T(x, y, u, v, u_{xc}, v_{xc}, \lambda)^{null} dx dy}{\int \int I(x, y, \lambda) \cdot T(x, y, u, v, u_{xc}, v_{xc}, \lambda)^{peak} dx dy} \quad (5)$$

where the double integral is performed over the KIN field-of-view, set by the the half-pupil PSF, as described above.

In order to provide some physical intuition, we note that for an object of angular size much smaller than the fringe spacing of the long baseline, the nulled signal would ideally be zero, resulting in  $L = 0$ . If, on the other hand, the object is large and its brightness distribution spans many long baseline fringes, the flux transmitted at null or at peak are similar and  $L = 1.0$ . Detailed descriptions of the theory behind the nuller measurement may also be found in Traub & Oppenheimer (2010) and Serabyn et al. (2011).

### 3.3. Data Reduction, Calibration and Errors

End-to-end data reduction and calibration was performed by the Keck Interferometer Project using their pipeline and external calibration package (*nullCalib*<sup>2</sup>). Here we summarize the steps involved and the various sources of measurement error.

During observing, a micro-sequence is executed during which the short baseline optical path modulation is always active (one fringe measurement every 25 msec), and the nullers alternate between the null and peak states (for 250 msec and 50 msec, respectively).

---

<sup>2</sup><http://nexsci.caltech.edu/software/V2calib/nullCalib/>

Depending on the object brightness, this sequence is repeated for 10–15 min, thus many thousand independent estimates of the leak are formed for each observation. From the scatter of these measurements a “formal” error is estimated for the average leak measurement corresponding to each observation.

Following standard practice, in order to monitor and subtract the instrument’s transfer function (i.e. the non-zero leak that is measured when observing a point source located at the phase center), observations of targets of interest were interleaved with observations of calibrator stars of known N-band angular diameters. Thus, the calibrated leak is:

$$L_{calibrated} = (L_{raw}^{target} - L^{system}) \tag{6}$$

where  $L^{system}$ , at the time of the target observations, is obtained by interpolation from the net leak measurements of the bracketing calibrator stars, after subtracting the calibrator leak expected given its angular diameter. This calculation is described in more detail in Appendix C of Colavita et al. (2009), and all the steps are applied by the package *nullCalib*.

The required calibrator angular diameters were measured using the simultaneous K-band fringe tracker data, and converted to N-band diameters using standard limb-darkening relations. The procedure is described in detail in Appendix A of Colavita et al. (2009); for clarity we repeat here some of the most relevant aspects. The approach was to treat the nulling targets as calibrators, since at K-band they are expected to effectively be simple naked stars. Although some of the calibrators are small ( $< 1$  mas) compared to the KI resolution, for such small calibrators the 20–30% precision obtained in those cases results in uncertainties on the calibrated leaks well below the leak measurement errors (best-case 0.2%, see below). At the other end of the size range, for a 3 mas calibrator, the largest in our sample, the diameter only needs to be known with 10% precision or better in order to not add significant error to the calibrated leaks. Thus, the calibration procedure is largely

insensitive to reasonable errors in the adopted calibrator angular diameters. The accuracy of our measured calibrator angular diameters was evaluated against estimates obtained using surface brightness relations; in all cases the discrepancies also result in a calibrated leakage differences smaller than the best-case measurement error. The uncertainties in the calibrator diameters are taken into account and propagated into the formal error of the calibrated leaks. The relevant parameters for the calibrators used for our sample are listed in Table 2.

We note that we make the assumption that there is no source of calibrator leak other than its angular extent, i.e. the calibrators have no excess N-band emission, which if unaccounted for would directly lead to underestimated exozodi emission levels. However, of 56 calibrators used in this study, one is a main-sequence star and all others are giants (i.e. none are super-giants), and all but three have spectral types K0–M0; both of which minimize the possibility of infrared emission above photospheric levels (e.g. Cohen et al. 1999, and references therein). Furthermore, all the calibrators used have been selected to have IRAS  $12\mu\text{m}/25\mu\text{m}$  flux ratios that agree, within the photometric errors, with that of a blackbody of the calibrator effective temperature. These methods, however, do not insure that our calibrators are free from low level dust emission at N-band (few percent or less), undetected in the K-band diameter comparisons and IRAS flux ratios. But we can use our own data to place some limits on the possible level of exozodi emission around our calibrators. Indeed, if calibrator exozodi emission were high, and variable from star to star, this would be apparent in correspondingly large leak fluctuations among the different calibrators. Specifically, we have compared the variations in system leak estimates made when same calibrator is used on either side of the target observation (only instrument variations expected) with the same quantity computed when two different calibrators are used (variations due to instrument plus calibrator exozodi level). Within measurement errors, we see no difference between those two cases, implying that our calibrators do not

contain large amounts of exozodi dust (in the language of Section 5,  $\lesssim 100$  zodi impact on average on the exozodi levels derived for the target stars).

We also include “external” errors in the calibrated leaks, which have been estimated from the night-to-night repeatability of multiple sets of calibrated data taken on the same star (Colavita et al. 2009, 2010). In summary then, the errors on  $L_{calibrated}$  contain two terms: (a) a formal error derived from the scatter of the leak measurements in each observation, and which also contains the uncertainties associated with the estimate of the system leak (mainly due to calibrator diameter uncertainties), and (b) the external error just described. Table 3 shows the measured calibrated leak and errors for each observation. As can be seen, for the stars in our sample the formal error is typically  $\sigma_{L_{calibrated}}^{formal} = 0.001$  to  $0.004$ . The external errors are wavelength and flux dependent; for the stars in our sample they are in the range:  $\sigma_{L_{calibrated}}^{ext.} = 0.002$  to  $0.0035$ .

Validation of the KIN response and calibration was evaluated by the project using a test system for which the expected leak could be calculated; in this case a binary system with a well known orbit (Appendix B of Colavita et al. 2009).

Table 3 also contains the calculated leak expected from the target star itself ( $L_{\star}$ ), which is needed in order to derive the excess leak due to the exozodi cloud, as described below. The calibrated leak data are also shown in Figure 2. We emphasize that at this stage we do not average the multiple leak measurements that are available for a given target, because variations among leaks measured at various times may in principle contain a contribution from the changing projected baseline fringe spacing and orientation. Thus we first model our measurements for a specific exozodi model, and average the results after this conversion, as described in Section 4.4. Figure 3 also summarizes our measurements but only for the wideband ( $8 - 9 \mu\text{m}$ ) channel used in the analysis presented here.

## 4. Data Modeling

### 4.1. Modeling Exozodi Clouds

In order to interpret our measurements and compare them to the Solar System case, we use the *Zodipic* code<sup>3</sup> to create images of zodi clouds around each of our targets. *Zodipic* synthesizes brightness distributions of exozodiacal clouds based on the empirical fits to the observations of the solar zodiacal cloud made by COBE (Kelsall et al. 1998).

When *Zodipic* generates a model brightness distribution for a zodi disk analog around a star other than the Sun, the dust has the same optical depth at 1 AU and radial density profile as in the Solar System. As a convenient unit, we refer to this model as corresponding to “1-zodi”, which we denote  $z = 1$ . *Zodipic* scales the radial temperature profile with stellar luminosity, and the inner dust radius is set by a dust sublimation temperature set at 1500 K (the dust inner radius is thus dependent on stellar spectral type, but  $z = 1$  models around any star have a fractional dust luminosity  $L_{dust}/L_{\star} \simeq 10^{-7}$ , the Solar System value). In the *Zodipic* code the dust density can be treated as a free parameter, allowing to generate brightness distributions for scaled version of the Solar System (the total flux due to the circumstellar dust scales linearly with  $z$ ). In the next section, we describe our procedure for converting the calibrated leaks to an exozodi dust density, parametrized in terms of a number ( $z$ ) of zodis.

We note that the zodiacal models used here include only the smooth component of interest, i.e. the Earth trailing blob and asteroidal dust bands are not included. We also note that increasing the optical depth of the cloud increases the collision rate, which affects the cloud structure, a physical process which is not taken into account by *Zodipic*. In a zodiacal cloud, grain–grain collisions become important for grains above a critical size,

---

<sup>3</sup><http://ssc.spitzer.caltech.edu/dataanalysistools/tools/contributed/general/zodipic/>

$\sim 30 - 150 \mu\text{m}$  in the solar zodiacal cloud (Fixsen & Dwek 2002), and which scales inversely as the optical depth of the disk (Kuchner & Stark 2010). Since this critical grain size reaches  $10 \mu\text{m}$  for a disk with about 3–15 zodis worth of dust, we expect that disks with more than roughly a few tens of zodis should begin to show morphological changes at KIN wavelengths because of the collision destruction of grains in the center of the disk. Our models, from *Zodipic*, are strictly linear in the dust density, and do not take this collisional depletion into account; this level of analysis is left to future studies.

We also note that our procedure assumes that the exo-zodi density in the inner-most regions of KIN sensitivity ( $\sim 10$  mas or 0.1 AU at 10 pc, as described above) follows the same radial density profile of the Kelsall et al. (1998) model, which was based on COBE/DIRBE measurements made at larger stellocentric radii, 0.9 AU or larger. However, measurements of the Solar zodiacal cloud made by the Helios probes as close as 0.3 AU (Leinert et al. 1981), and measurements in the solar F corona (MacQueen & Greeley 1995), both find radial density profiles with exponents of  $\sim 1.3$ , in agreement with the Kelsall et al. (1998) model.

The *Zodipic* images generated are  $512 \times 512$  pixels, with a scale of 2 mas/pixel, i.e.  $10\times$  finer than the long baseline fringe spacing. The image size is thus  $1024 \times 1024$  mas, a good match to the KIN field-of-view (given by  $T_{PSF}$ ). Figure 1 includes an example *Zodipic* image for a Solar System analog at 10 pc. We note that this image size (in pixels) keeps the computation times short, but at this spatial resolution the stellar disk would not be well sampled. Therefore, the *Zodipic* images generated do not include the central stars, they represent only the exozodi brightness distribution ( $I_{zodi}$ ).

## 4.2. From Calibrated Leak to Number of Zodis

If we decompose the total brightness distribution into that of the central star and the exozodi cloud,  $I = I_\star + I_{zodi}$ , it follows that:

$$\begin{aligned} L_{calculated}^{zodi} &\simeq \frac{\int \int I_{zodi}(x, y, \lambda) \cdot T(x, y, u, v, u_{xc}, v_{xc}, \lambda)^{null} dx dy}{\int \int I_\star(x, y, \lambda) \cdot T(x, y, u, v, u_{xc}, v_{xc}, \lambda)^{peak} dx dy} \\ &= \frac{\int \int I_{zodi}(x, y, \lambda) \cdot T(x, y, u, v, u_{xc}, v_{xc}, \lambda)^{null} dx dy}{F_\star} \end{aligned} \quad (7)$$

where the approximation holds when the stellar flux ( $F_\star$ ) dominates over the exozodi flux, which is always the case here. The calculation is made monochromatically, at the effective wavelength ( $8.5 \mu\text{m}$ ) of the  $8 - 9 \mu\text{m}$  spectral bin used. The error introduced by this approximation is negligible, at the level of a fraction of a zodi, compared with typical 100s of zodi errors from the formal and external leak errors.

Thus, we also remove the stellar contribution from the measured calibrated leak:

$$L_{measured}^{zodi} = (L_{calibrated} - L_\star) \quad (8)$$

where the leak due to the central star (Table 3) is calculated using an estimate of its angular diameter, following Serabyn (2000):

$$L_\star \simeq \frac{\pi^2}{16} \cdot \left( \frac{B_p(m) \cdot \theta_\star(\mu\text{rad})}{\lambda(\mu\text{m})} \right)^2 \quad (9)$$

where  $B_p$  is the length of the projection of the baseline on the sky in the direction to the star and  $\theta_\star$  is the stellar disk angular diameter (Table 1). We note that in the above expression we have neglected limb-darkening terms, unimportant for the spectral type and luminosity class of the stars in our sample.



Equation 8 illustrates an important advantage of the KIN measurements compared to spectro–photometric flux excess measurements which require accurate calibration of the stellar photosphere flux level: the excess leak ( $L_{measured}^{zodi}$ ) estimate depends only on the stellar leak estimate ( $L_{\star}$ ), which is easy to determine given the spectral types of the stars in our sample. Furthermore, the stars are generally small ( $\sim 1$  mas, Table 1) compared to the KIN resolution at  $8.5 \mu\text{m}$ . Therefore the correction is small and the uncertainty in the stellar angular diameters affects very weakly the uncertainty on  $L_{\star}$  and on  $L_{measured}^{zodi}$ .

For each target and for each individual observation, our procedure consists of the following steps:

1. Compute the measured excess leak  $L_{measured}^{zodi}$ . The uncertainty in the angular diameter of each of our target stars propagates into the uncertainty in the excess leak.
2. For a given exozodi disk orientation (inclination  $i_{disk}$  and position angle  $\text{PA}_{disk}$ ), compute  $L_{calculated}^{zodi}$  for a *Zodipic* model which has a dust density (number of zodis,  $z$ ) such that the measured excess leak is matched:  $L_{calculated}^{zodi} = L_{measured}^{zodi}$ . Derive uncertainties in the required number of zodis from the formal and external errors. As noted earlier, this conversion to number of zodis must be made for each observation, because the instantaneous KIN fringe pattern that corresponds to each observation must be applied when using Equation 7.
3. Repeat for a range of disk inclinations and position angles which span the extremes in predicted leak; namely: face–on ( $i_{disk} = 0^\circ$ ) and edge–on ( $i_{disk} = 90^\circ$ ) with position angle parallel and perpendicular to the instantaneous direction of the long baseline fringes. In our averaging scheme, described below, we will take the variation resulting from the uncertainty in the exozodi cloud orientation as an additional source of error in the derived numbers of zodis. We note that (as can be seen in Table 4) in most

cases the resulting uncertainty is significantly smaller than that due to the formal and external errors. As described in Section 5, for  $\eta$  Crv and  $\gamma$  Oph, imaging observations have constrained the inclination and position angle of the outer disk, and in those cases we also derive the number of zodis implied by our measurements by assuming that the exozodi disk has the same orientation as the outer disk.

Table 4 shows our results in terms of number of zodis ( $z_{ij}$ ) for each observation and for each disk orientation. The notation refers to observation  $i$  in “cluster”  $j$ . The notion of cluster must be introduced now in order to properly account for the external error in the averaging process described below. KIN observations of a given target begin with an adjustment to the static internal optical delay, and an on-sky alignment procedure which maximizes the mid-infrared flux seen by the nulling camera. We call a cluster a certain number of observations (typically 1 – 4) of the same target in between such changes to the instrument setup. Clusters of observations of the same target may be made during the same night, or on distinct nights. Table 4 also shows the error in the number of zodis that result from the formal and external leak errors ( $\sigma_{ij}^{formal}$  and  $\sigma_j^{ext}$ ) as well as the error due to the uncertainty in the stellar leak ( $\sigma^*$ ). We note that although unphysical, negative zodis are allowed as a result of the error bars on the leak measurements. Finally, in order to describe the spatial extent of the exo-zodi region that the KIN is most sensitive to, the last column of Table 4 gives the half-light radius ( $R_{\text{half-light}}$ ) of the azimuthally averaged exo-zodi brightness transmitted through the KIN fringe pattern. These radii may be compared, for example, to the radii of center of habitable zone given in Table 1.

### 4.3. Special Cases

#### 4.3.1. *Altair ( $\alpha$ Aql)*

As mentioned above, the stellar diameters of our target stars are generally small, resulting in small errors in the stellar leak corrections. The exception is Altair ( $\alpha$  Aql) which is large enough that uncertainties in its angular diameter can result in a significant uncertainty in the estimate of the excess leak. In order to estimate the stellar leak for this star, we use the image of its (elongated) photospheric disk made at the CHARA array (Monnier et al. 2007). The position angle of the KI baseline at the time of our observations ranged from  $36^\circ$  to  $41^\circ$ , approximately the same as the position angle of the major-axis of the CHARA image. Therefore, we use their measurement of the equatorial diameter ( $3.6 \pm 0.016$  mas) in order to predict and correct for the stellar leak ( $L_\star = 0.0172 \pm 0.00015$  and  $0.0179 \pm 0.00015$ , for our UT 2008 June 25 and 26 epochs respectively).

#### 4.3.2. *Binaries*

As can be seen in Table 1, five of our targets are known to have stellar companions (Kx Lib, 70 Oph,  $\iota$  Peg, 61 Cyg A and 107 Psc). Therefore, we must evaluate their possible contribution to the measured leak, and correct for it if needed.

Two of those stars, Kx Lib and 70 Oph, have their companions at separations of 25 and 5 arcsec respectively, well outside the KIN field-of-view, and therefore have no impact on the measured leak.

For  $\iota$  Peg, we have used the orbit of Boden et al. (1999) to determine the companion location at the epochs of our observations. We compute the leak due to the primary+secondary stellar system using the primary and secondary stellar angular

diameters of Boden et al. (1999) and a primary/secondary flux ratio of 4.0 at  $8.5\ \mu\text{m}$ , also estimated using the stellar diameters and effective temperatures derived by Boden et al. (1999). This results in a stellar leak (both components) of  $L_\star = 0.0152$  and  $0.0153$  for the 14 July 2008 UT = 14.24 and 14.95 epochs, respectively.

For 61 Cyg A and 107 Psc, we also use published orbits (from the Sixth Catalog of Orbits of Visual and Binary Stars, by W. I. Hartkopf and B. D. Mason<sup>4</sup>) to compute the companion locations at the epochs of the KIN observations. These companions are inside the KIN FOV. However, we have found no information from which the components flux ratio could be derived. Therefore, we perform no correction for these systems, and the results presented here in terms of zodi limits are to be considered upper-limits (i.e. any subtraction from the measured leak due to the companion would result in a smaller inferred exozodi level).

#### 4.4. Averaging Scheme

After converting each leak measurement to a number of zodis we average the multiple observations available for each target in order to reduce the measurement errors. Consistent with the characterization of the external error described in Colavita et al. (2009, 2010), we average observations and clusters as follows:

1. Within each cluster: Compute the weighted mean of the number of zodis,  $z_j = \sum(z_{ij} \cdot w_{ij}) / \sum w_{ij}$ , where the formal errors provide the weights,  $w_{ij} = 1.0/\sigma_{ij,formal}^2$ . The error in the weighted mean is taken to be the largest of the statistical error in the mean ( $\sigma_{z_j}^a = 1.0/\sqrt{\sum w_{ij}}$ ) and the weighted average standard deviation in the

---

<sup>4</sup><http://ad.usno.navy.mil/wds/orb6.html>

data ( $\sigma_{z_j}^b = \sqrt{\frac{\sum (z_{ij} - z_j)^2 \cdot w_{ij}}{\sum w_{ij}}}$ ). To this error we add the external error in quadrature:  
 $\sigma_{z_j} = \sqrt{\sigma_{j,ext}^2 + \max\{\sigma_{z_j}^a, \sigma_{z_j}^b\}^2}$ .

2. To combine the clusters: we again compute the weighted mean ( $\bar{z} = \frac{\sum (z_j \cdot w_j)}{\sum w_j}$ , with  $w_j = 1.0/\sigma_{z_j}^2$ ), and the error in the weighted mean given by the statistical error ( $\sigma_{\bar{z}} = 1.0/\sqrt{\sum w_j}$ ).

We note that these first two steps imply that (a) the total error per cluster can never be smaller than the external error, and (b) when averaging multiple clusters, the total error can become smaller than the external error. The latter however generally provides only a small improvement, because our data sets for each target contain only 1 or 2 clusters.

3. The steps above are done for each exozodi orientation, the last step is to average the results over the 3 disk orientations computed ( $i_{disk} = 0^\circ$  and  $i_{disk} = 90^\circ$  with  $PA_{disk}$  parallel or perpendicular to the instantaneous long baseline fringes). Thus, the final error contains a term (added in quadrature) computed as the rms of the number of zodis deduced for the 3 disk orientations ( $\sigma_{[i_{disk}, pa_{disk}]}$ ). As mentioned above, the “disk orientation error” is typically relatively small, tens of zodis, compared to that resulting from the formal and external error sources. The final number of exozodis for each target, including all data points and uncertainties is:  $z = \sum_1^3(\bar{z})/3$ ,  
 $\sigma_z = \sqrt{\sigma_{\bar{z}}^2 + \sigma_{[i_{disk}, pa_{disk}]}^2}$ .

## 5. Results

Our final average results per target ( $z, \sigma_z$ ) are shown in Table 5. The table also shows the detection significance in each case, as well as  $3\sigma$  upper-limits, for ease of comparison with previous surveys that use similar metrics. These results are also illustrated in Figure 4.

### 5.1. $\eta$ Crv

Our only significant detection is  $\eta$  Crv ( $1250 \pm 260$  zodis). This object was previously known to have high levels of circumstellar dust, including observations with Spitzer/MIPS at  $70 \mu\text{m}$  (Beichman et al. 2006b), Spitzer/IRS/ at  $10 - 35 \mu\text{m}$  (Chen et al. 2006) and VLTI/MIDI at  $10 - 13 \mu\text{m}$  (Smith et al. 2009). Also, as can be seen in Figure 2, the KIN spectrum across the N-band has adequate SNR to resolve the  $10 \mu\text{m}$  silicate feature and can be used to infer dust properties. A detailed analysis of these data is left to future work.

The outer disk in this object has been directly imaged (Wyatt et al. 2005; Matthews et al. 2010). Thus, instead of taking the disk inclination and position angle as free parameters, we may assume that the exozodi disk has the same orientation. Using the parameters from the Matthews et al. (2010) Herschel observations ( $i_{disk} = 50^\circ$  with  $\text{PA}_{disk} = 103^\circ$ ), we find  $z = 1300 \pm 160$ .

### 5.2. $\gamma$ Oph

This star was previously known to have excess starting at  $15 \mu\text{m}$ , and growing much larger at longer wavelengths (Su et al. 2008). It is noteworthy that the infrared excess luminosity is several times larger for  $\gamma$  Oph than for  $\eta$  Crv, while the KIN makes a clear detection for  $\eta$  Crv but only a marginal detection ( $\sim 2.6\sigma$ ) for  $\gamma$  Oph; implying perhaps that the dust distributions are very different in these two objects.

The Spitzer images spatially resolve the outer disk, and imply  $i_{disk} = 50^\circ$  and  $\text{PA}_{disk} = 55^\circ$ . Assuming the same orientation for the exozodi disk we derive  $z = 200 \pm 60$ .

### 5.3. $\alpha$ Aql (Altair)

This star was not previously known to have warm circumstellar dust. The KIN results indicate a marginal detection ( $3.0\sigma$ ). The KIN measures an excess leak of  $\sim 0.8\%$ . This level of excess would have been undetectable by IRAS at  $12\mu\text{m}$ , and no  $8\mu\text{m}$  excess measurements have been made with Spitzer. Therefore, assuming the dust temperature is relatively warm, a KIN detection would not be inconsistent with the lack of excess seen in previous measurements.

### 5.4. Non-detections

Excluding our only clear detection ( $\eta$  Crv) and the two possible detections ( $\gamma$  Oph and  $\alpha$  Aql), our sample contains 22 non-detections. Table 5 shows the upper limits on the number of zodis for each star that can be derived from our measurements. The average  $3\sigma$  upper limit is 570 zodis. We note that the weighted RMS data scatter for the non-detections (150 zodis) is similar to the mean data uncertainty (160 zodis), which we take as an indication that the errors in the individual measurements have been fairly assigned.

## 6. Discussion and Conclusions

### 6.1. Comparison with Spitzer/IRS

Spitzer/IRS established exozodi limits based on fractional excess flux measurements ( $F_{dust}/F_{\star}$ ) made in the  $8.5 - 12\mu\text{m}$  band (Beichman et al. 2006a; Lawler et al. 2009). Using a sample of 203 stars, the detection rate was only 1%. Based on their estimated error in the measurement of the fractional excess fluxes of  $\sim 1\%$  ( $1\sigma$ ), the sample of non-detection

was used to place  $3\sigma$  limits on the number of zodis in the range 600 – 2700 zodis, with an average of 1100 zodis. Because the IRS short wavelength band is very similar to that of the KIN, it is of interest to compare the results from the two surveys.

First, we note that the KIN measurement can also be expressed in terms of a fractional flux excess measurement; which enables a direct comparison of expected performances (the much larger FOV of Spitzer/IRS is not expected to enter the comparison, because dust located outside the KIN FOV will be too cold to significantly contribute N–band flux). Assuming perfect stellar cancellation, the numerator in Equation 5 (i.e. at null) equals a fraction  $f$  of the zodi flux  $F_{dust}$ , where  $f$  is the instantaneous fraction of the zodi flux removed by the KIN fringe pattern at null. Likewise, since  $F_{\star} \gg F_{dust}$ , the denominator (i.e. at peak) is essentially equal to the flux from the central star, therefore:

$$\frac{F_{dust}}{F_{\star}} \simeq \frac{L}{f} \tag{10}$$

and the error on this estimate of the fractional flux excess obtained from the KIN data is:

$$\sigma\left(\frac{F_{dust}}{F_{\star}}\right) \simeq \frac{\sigma_L}{f} \tag{11}$$

The factor  $f$  can be easily computed for each observation as the ratio of the exozodi flux transmitted through the KIN pattern at null to the total exozodi flux (for any value of  $z$ , say  $z = 1$ ). On average,  $f = 0.4$ , and varies by less than 5% for our sample, including the exozodi cloud orientation effects (inclination and position angle, relative to the KIN fringe pattern). Therefore, in this conversion, the KIN measurement errors,  $\sigma_L = 0.002$  to  $0.004$ , are degraded by a factor of  $1/f \simeq 2.5$ , to become  $\sigma\left(\frac{F_{dust}}{F_{\star}}\right) = 0.005$  to  $0.0075$ . This is to be compared with the best–case IRS errors,  $\sigma\left(\frac{F_{dust}}{F_{\star}}\right) = 0.01$ . It follows that one



expects the current KIN implementation to provide up to  $\times 2$  tighter exozodi limits than Spitzer/IRS. We note however that the errors quoted for Spitzer/IRS do not include possible and potentially significant systematic errors arising from uncertainties in the absolute calibration of the stellar flux, to which the KIN is immune, as described earlier. In that sense, the above comparison represents a lower bound to the improvement that can be expected from the KIN.

Table 6 summarizes the detailed comparison of exozodi limits for the eight objects in common between the Spitzer/IRS and KIN surveys. It can be seen that on a target-by-target basis, either Spitzer/IRS or KIN can provide tighter limits, depending on the precise measurement errors in each case; but that we recover a common  $2\times$  improvement from KIN, as predicted.

## 6.2. Population Analysis

Having determined exozodi limits for each star in our sample, we now interpret those observations in terms of a statistically-defined exozodi disk model, in order to extract as much information as possible from the KIN measurements. Noting that the measured values in Table 5 tend to scatter around zero, and that the typical uncertainties are large compared to most of the measured values, and certainly large compared to the average of the measured values, we consider in this section the possibility that the true underlying exozodi values might be significantly smaller than the upper limits implied by the individual measurements.

For this analysis, we define the sub-sample of  $N = 23$  stars which were not previously known to contain circumstellar dust (excludes  $\eta$  Crv and  $\gamma$  Oph). We assume that this sub-sample is representative of a single class of stars, with respect to the level of warm

exozodi emission. In Appendix A we show that the calibrated net leaks are not correlated with any of the parameters in an exhaustive list describing the instrumental conditions. Furthermore, correlations are not expected among targets. Therefore, we assume that the zodi levels inferred for each star form an uncorrelated set, and that it is thus appropriate to use the 23 measurements to estimate the mean zodi level and its error for the class. We choose the bootstrap method to form a robust estimate of the mean and its error, independent of any assumptions on the underlying statistics (Efron & Tibshirani 1998); using with  $10^6$  re-samples of the set of 23 measurements we find  $\hat{z} = +2 \pm 50$  ( $1\sigma$  error)<sup>5</sup>.

Further interpretation of this result, in terms of a confidence level for the mean exo-zodi emission for the class being below a certain level, would require knowledge, which we do not have, of the underlying probability distribution for the measurement errors (i.e. whether or not they are approximately Gaussian) and of the underlying distribution of exo-zodi levels for the class of stars represented by our sample. If the measurement errors were Gaussian, the above result would imply that the mean exo-zodi level for the class is  $< 50$  zodis ( $1\sigma$  upper limit) with 84% confidence, or  $< 150$  zodis ( $3\sigma$  upper limit) with 99.8% confidence. Moreover, as detailed in Appendix B, we have also used Monte-Carlo simulations, and a wide range of assumed exo-zodi distribution, to show that these conclusions are largely insensitive to the shape and mean level of the true underlying exo-zodi distribution.

---

<sup>5</sup>This estimate of the error in the mean agrees well with one computed instead as the weighted RMS (170) divided by  $\sqrt{\text{EDOF}}$ , resulting in  $\sigma_z = 58$ , and where EDOF is the equivalent degrees of freedom which takes into consideration the data weights ( $w_i$ ),  $\text{EDOF} = (\sum w_i)^2 / \sum (w_i^2) = 9$ .

### 6.3. Conclusions

Both our limits on individual stars, and the statistical result just discussed, are very positive for the future of direct imaging of exoplanets in the habitable zones around nearby stars, since they suggest that the exozodi levels might not be as high as was once feared. However, to be able to detect an exoEarth with any technique, the noise in a resolution element stemming from exozodi emission must be no more than a few Earth fluxes; and the limits presented here could still allow actual exozodi levels well above what can be tolerated. Measurements with sensitivity to lower exozodi levels are thus needed. The next step will likely be enabled by the Large Binocular Telescope Interferometer (LBTI), which will also use the nulling technique at mid-infrared wavelengths (Hinze 2009). Beyond that, a dedicated space mission, and multi-wavelength characterization, might be required.

#### A. Correlation Analysis

In order to validate our noise model, we have examined the dependence of the calibrated net leaks (i.e. stellar contribution subtracted) against a set of 26 variables describing the instrumental and environmental conditions, and the astrophysical properties of the target stars and associated calibrators. For this study, we have selected the (68) independent measurements corresponding to the sub-sample of 23 stars not previously known to contain circumstellar dust (excludes  $\eta$  Crv and  $\gamma$  Oph). The independent variables considered are: (1) day of year, (2) local time, (3) hour angle, (4) telescope azimuth, (5) telescope elevation, (6) internal optical delay difference, (7) right ascension, (8) declination, (9) stellar age, (10) stellar effective temperature<sup>6</sup>, (11) detected N-band flux, (12) detected K-band

---

<sup>6</sup>To be sure, the measured leaks can be expected to correlate with stellar properties such as age or effective temperature; those parameters are tested in the event that they indirectly

flux (fringe tracker), (13) detected J–band flux (angle tracker), (14) angle tracker centroid RMS, (15) percent of leak data accepted by the quality gates, (16) precipitable water vapor (PWV), (17) wind speed, (18) wind direction, (19) air temperature, (20) relative humidity, (21) atmospheric pressure, (22) coherence time due to dry air (as in Colavita 2010), (23) coherence time due to water vapor (as in Colavita 2010), (24) calibrator diameter, (25) target–calibrator angular separation, and (27) target–calibrator flux ratio. The simultaneous PWV measurements are from the Caltech Submillimeter Observatory (CSO) tau–meter archive. All other atmospheric quantities are from the Canada–France–Hawaii Telescope (CFHT) weather archive.

Visual inspection of the correlation plots reveals that a linear relation would be sufficient to describe any candidate correlation. In order to obtain robust estimates of the statistical significance of any correlation candidate, we adopt a bootstrap approach. For each item, we perform a linear fit for each of  $10^6$  bootstrap re–samples of the data. For each item, the mean of the  $10^6$  fitted slopes is a good estimate of the slope; and the standard deviation is a good estimate of its uncertainty, independent of any assumptions on the underlying statistics (Efron & Tibshirani 1998). The ratio of the mean slope and error thus represents the significance of the slope being different from zero.

The result is that for most items (23 of the 26) the slope deviates from zero at a level less than  $1\sigma$ ; and for all items the deviation is less than  $2\sigma$ . We therefore conclude that there are no statistically significant correlations in our data between the calibrated net leaks and any of the instrument/environment/astrophysical parameters that we have considered.

---

reveal a correlation with an instrument condition.

## B. Dependence of the mean exo-zodi confidence intervals on the underlying exozodi distribution

In order to determine the precise meaning of the error in the mean exo-zodi level calculated in Section 6.2, and to determine its dependence on the shape of the underlying distribution describing the number of stars with a certain exo-zodiacal level, we consider two illustrative examples: a uniform distribution ( $f(z) = 1$  for  $z$  in the interval  $[0, 2\bar{z}]$ , and 0 otherwise), and a half-exponential function ( $f(z) = e^{-z/\bar{z}}$  for  $z$  in the interval  $[0, \infty]$ ), where  $\bar{z}$  is the true mean exozodi level. We consider those distributions over a large range of  $\bar{z}$  values, from 1 to 1000 zodis. The shapes of those two distributions (from completely flat to very centrally peaked) together with the large range of  $\bar{z}$  values explored ensures our conclusions are robust with respect to the range of possible exozodi distributions.

Our procedure is as follows: (a) assume one of the exozodi distributions, uniform or half-exponential; (b) assume a value of the true mean zodi for the distribution ( $\bar{z}$ ); (c) draw 23 random numbers ( $z_i$ ) from the resulting  $f(z)$  distribution; (d) simulate the measurement process by creating a simulated dataset by selecting 23 random numbers from normal distributions, of means =  $\{z_i\}$  (from step (c) above) and standard deviations =  $\{\sigma_z\}$  (the actual error on each exozodi datum); (e) compute the weighted mean and error in the mean for each set of simulated data; (f) repeat the simulation of the 23 measurements a large number of times ( $10^6$ ), and count the number of times that the simulated mean differs from the true exozodi value ( $\bar{z}$ ) by less than 1 or 2 times the error in the mean. The above procedure is repeated for  $\bar{z} = 1$  to 1000, and for both the uniform and half-exponential distributions.

By counting how many realizations of our simulated measurement process correspond to a true mean zodi value that lies within the range  $\pm n\sigma$  from the mean, we generate a probability that this event could occur. The results are shown in Figure 5 where this

probability is plotted for a range of true mean zodi values, and for both the uniform and an half-exponential distributions. These two distributions give essentially identical probabilities – 67% and 94% for 1 or  $2\sigma$ , respectively – for small values of the mean zodi level, and very similar results for larger values. This implies that the shape of the underlying distribution is not very important. We note that in Figure 5 the probability of the true mean value being in the indicated range falls off for large values of the true mean zodi. This is expected because in this case the distribution function is no longer being sampled densely enough over its whole range, so  $N = 23$  samples are not quite sufficient to define the mean value. However this part of the curve is not important to our conclusions, because our interest is at smaller values.

The Keck Interferometer is funded by the National Aeronautics and Space Administration as part of its Exoplanet Exploration Program. The data presented herein were obtained at the W.M. Keck Observatory, which is operated as a scientific partnership among the California Institute of Technology, the University of California and the National Aeronautics and Space Administration. The Observatory was made possible by the generous financial support of the W.M. Keck Foundation. The authors wish to recognize and acknowledge the very significant cultural role and reverence that the summit of Mauna Kea has always had within the indigenous Hawaiian community. We are most fortunate to have the opportunity to conduct observations from this mountain. This work has made use of services produced by the NASA Exoplanet Science Institute at the California Institute of Technology. This research has made use of the Washington Double Star Catalog maintained at the U.S. Naval Observatory. Part of this work was carried out at the Jet Propulsion Laboratory, California Institute of Technology, under contract with NASA. The authors wish to acknowledge invaluable contributions from the KI team at Keck Observatory, the Jet Propulsion Lab and the NASA Exoplanet Science Institute. RMG acknowledges fruitful

discussions with J. D. Monnier.

*Facilities:* Keck Interferometer.

## REFERENCES

- Absil, O. et al. 2008, *A&A*, 487, 1041
- Absil, O. et al. 2006, *A&A*, 452, 237
- Absil, O. et al. 2009, *ApJ*, 704, 150
- Akeson, R. L. et al. 2009, *ApJ*, 691, 1896
- Aumann, H. H. et al., 1984, *ApJ*, 278L, 23
- Backman, D. E. and Paresce, F. 1993, in *Protostars and planets III (A93-42937 17-90)*, p. 1253-1304
- Beckwith, S. V. W. 2008, *ApJ*, 684, 1404
- Beichman, C. A., et al. 2006a, *ApJ*, 639, 1166
- Beichman, C. A., et al. 2006b, *ApJ*, 652, 1674
- Boden, A. F. et al. 1999, *ApJ*, 515, 356
- Bryden, G. et al. 2006, *ApJ*, 636, 2, 1098
- Chen, C. H., et al. 2006, *ApJS*, 166, 351
- Cohen, M., Walker, R. G., Carter, B., Hammersley, P., Kidger, M. & Noguchi, K, 1999, *AJ*, 117, 1864
- Colavita, M. M., Serabyn, E., Ragland, S., Millan-Gabet, R., & Akeson, R. L., 2010, *Proc. SPIE*, 7734, 77340T
- Colavita, M. M., 2010, *PASP*, 122, 712
- Colavita, M. M., et al. 2009, *PASP*, 121, 1120



- Dermott, S. F., Nicholson, P. D., Burns, J. A. & Houck, J. R., 1984, *Nature*, 312, 505
- Efron, B. & Tibshirani, R. J. 1998, “An Introduction to the Bootstrap”, Chapman & Hall/CRC
- Fixsen, D. J. & Dwek, E. 2002, *ApJ*, 578, 1009
- Hinz, P. 2009, *AIP Proc.*, 1158, 313
- Holmber, J., Nordstrom, B. & Andersen, J., 2009, *A&A*, 501, 941
- Kalas, P. et al. 2008, *Science*, 322, 5906, 1245
- Kelsall, T. et al. 1998, *ApJ*, 508, 44
- Kuchner, M. J. & Stark, C. C. 2010, *ApJ*, 140, 1007
- Kuchner, M. J., Brown, M. & Koresko, C., 1998, *PASP*, 110, 1336
- Lawler, S. M. et al. 2009, *ApJ*, 705, 89
- Leinert, C., Richter, I., Pitz, E. & Planck, B., 1981, *Å*, 103, 177
- Liu, W. M. et al. 2004, *ApJ*, 610L, 125
- MacQueen, R. M. & Greeley, B. W., 1995, *ApJ*, 440, 361
- Matthews, B. C. et al., 2010 *A&A*, 518L, 135
- Mamajek, E. & Hillenbrand, L. A. 2008, *ApJ*, 687, 1264
- Marois, C., Macintosh, B., Barman, T., Zuckerman, B., Song, I., Patience, J., Lafreniere, D. & Doyon, R., 2008, *Science*, 322, 5906, 1348
- Mennesson, B., Leger, A. & Ollivier, M. 2005, *Icarus*, 178, Issue 2, 570

- Monnier, J. D. et al. 2007, *Science*, 317, 342
- Nesvorny, D., Jenniskens, P., Levison, H. F., Bottke, W. F., Vokrouhlicky, D. & Gounelle, M., 2010, *ApJ*, 713, 816
- Rhee, J. H., Song, I., Zuckerman, B. & McElwain, M., 2007, *ApJ*, 660, 1556
- Rieke, G. H. et al. 2005, *ApJ*, 620, 2, 1010
- Serabyn, E., 2000, *Proc. SPIE*, 4006, 328
- Serabyn, G. 2011, in preparation
- Smith, R., Wyatt, M. C. & Haniff, C. A., 2009, *A&A*, 503, 265
- Stark, C. C. et al. 2009, *ApJ*, 703, 1188
- Stark, C. C. and Kuchner, M. J. 2008, *ApJ*, 686, 637
- Su, K. Y. L., Rieke, G. H., Stapelfeldt, K. R., Smith, P. S., Bryden, G., Chen, C. H. & Trilling, D. E., 2008, *ApJ*, 679, L125
- Su, K. Y. L. et al. 2006, *ApJ*, 653, 1, 675
- Traub, W. A. and Oppenheimer, B. R. 2010, in “Exoplanets”, University of Arizona Press, Ed. S. Seager
- Valenti, J. A. & Fischer, D. A., 2005, *ApJS*, 159, 141
- Wolf, S., Moro-Martin, A. & D’Angelo, G., 2007, *Planet. Space Sci.*, 55, 5, 569
- Wright, J. T., Marcy, G. W., Butler, R. P. & Vogt, S. S., 2004, *ApJS*, 152, 261
- Wyatt, M. C. et al. 2005, *ApJ*, 620, 492
- Wyatt, M. C. 2008, *ARA&A*, 46, 339

Zuckerman, B. 2001, *ARA&A*, 39, 549

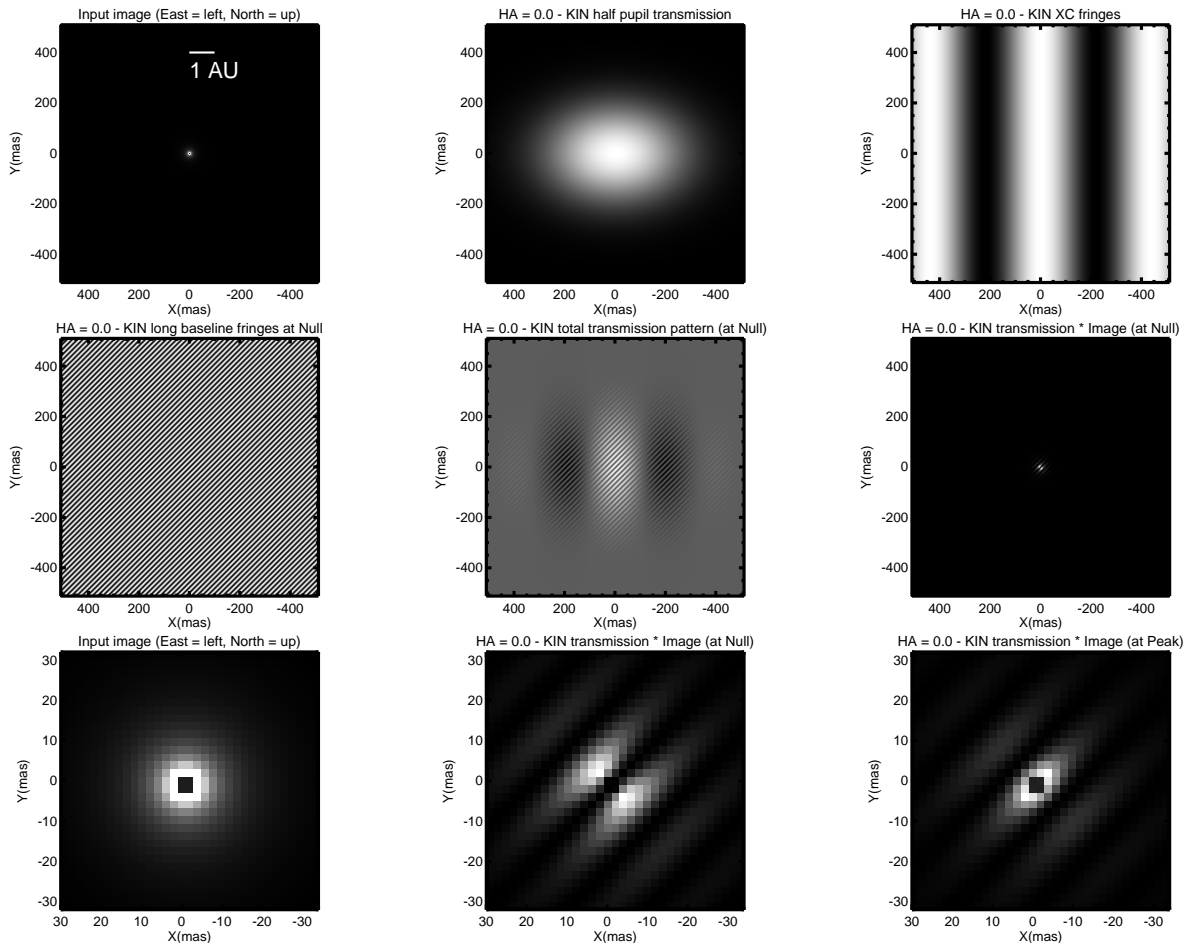


Fig. 1.— *Zodipic* image of a face-on Solar System analog at 10 pc, and KIN fringe patterns computed at  $8.5 \mu\text{m}$  for H.A.=0 and  $\text{dec}=20^\circ$ . In these images, the central star has been removed. Top-row: input image ( $I$ ), half-aperture PSF ( $T_{PSF}$ ), and short baseline fringes ( $T_{XC}$ ). Middle-row: long baseline fringes ( $T_{long}$ ), total transmission pattern (product of  $T_{PSF} \times T_{XC} \times T_{long}$ ), and total transmitted brightness ( $I \times T_{PSF} \times T_{XC} \times T_{long}$ ). Bottom-row: zoomed versions of the input image and transmitted brightness at null and peak.

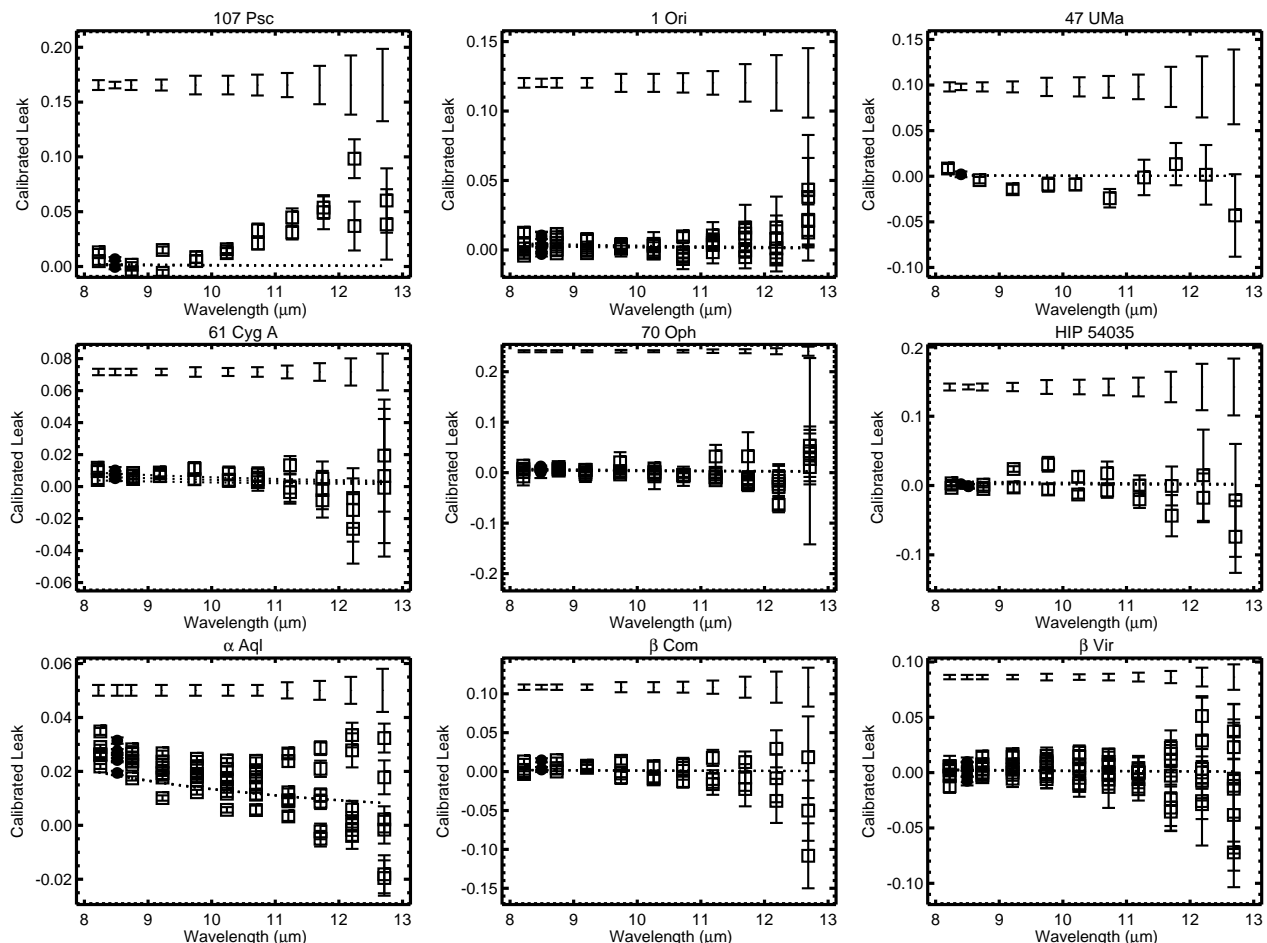


Fig. 2.— Calibrated leak data for all targets as a function of wavelength. Individual observations for each target, including formal errors, are shown as square symbols. The external errors for each target and at each wavelength are shown by the bars at the top of each plot. The leak level due to the central stars, and its uncertainty, are also shown (dotted lines). The degradation of the calibration quality at the red end of the bandpass, as discussed in the text, can be clearly seen. For the analysis presented in this paper we use only the  $8 - 9 \mu\text{m}$  spectral bin (solid circles), which has the highest sensitivity for exozodi detection.

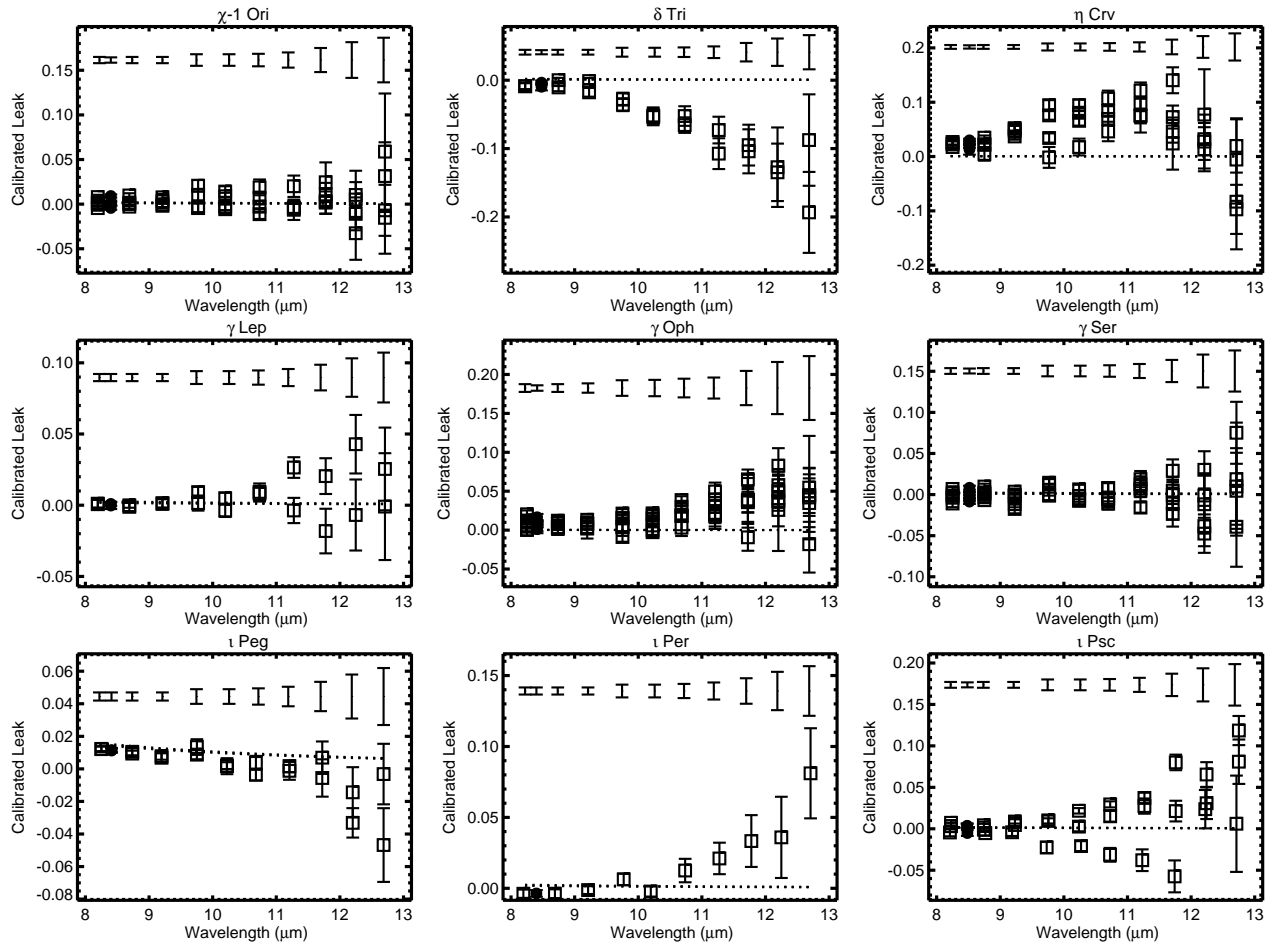


Fig. 2.— *continued*

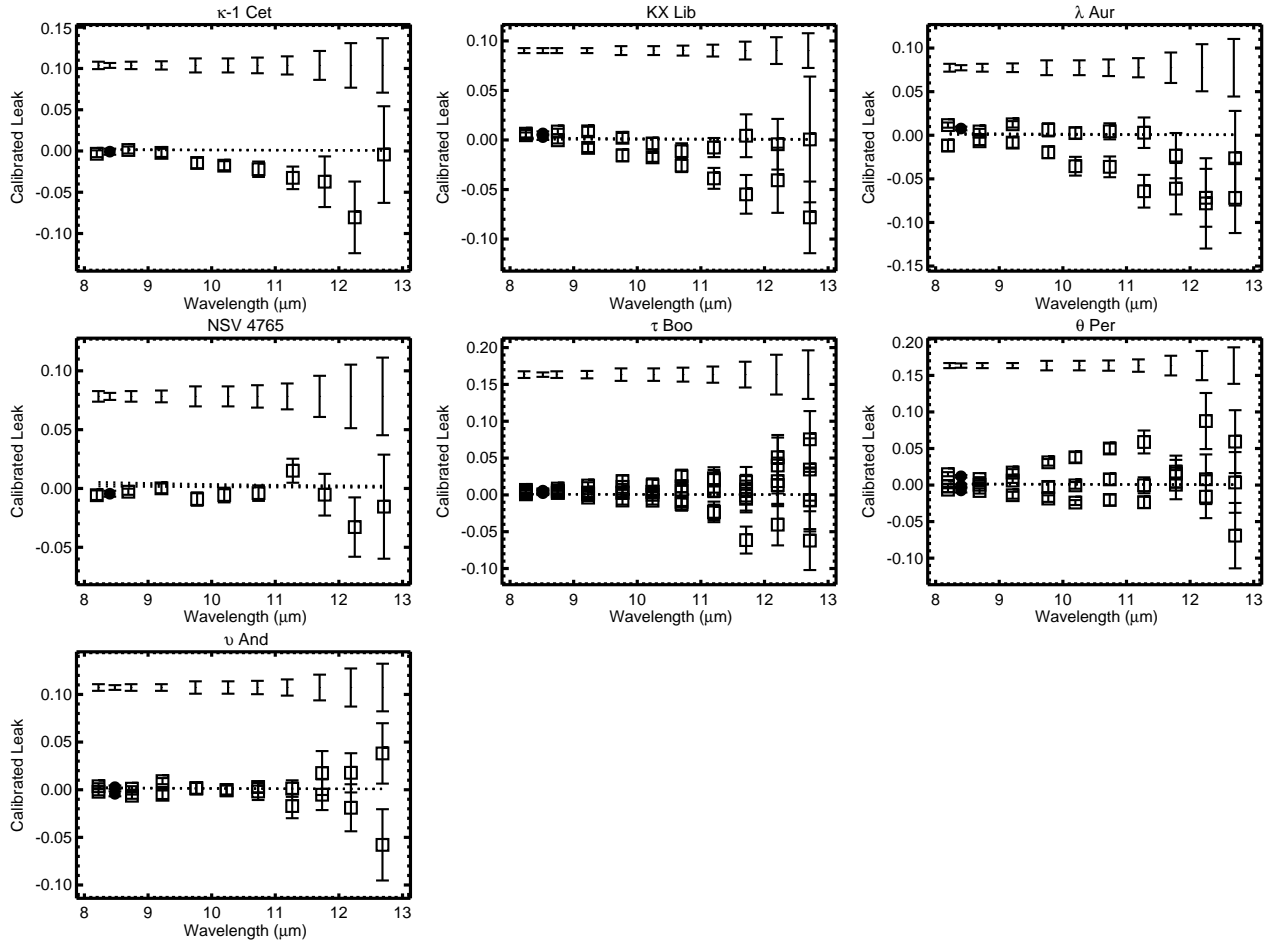


Fig. 2.— *continued*

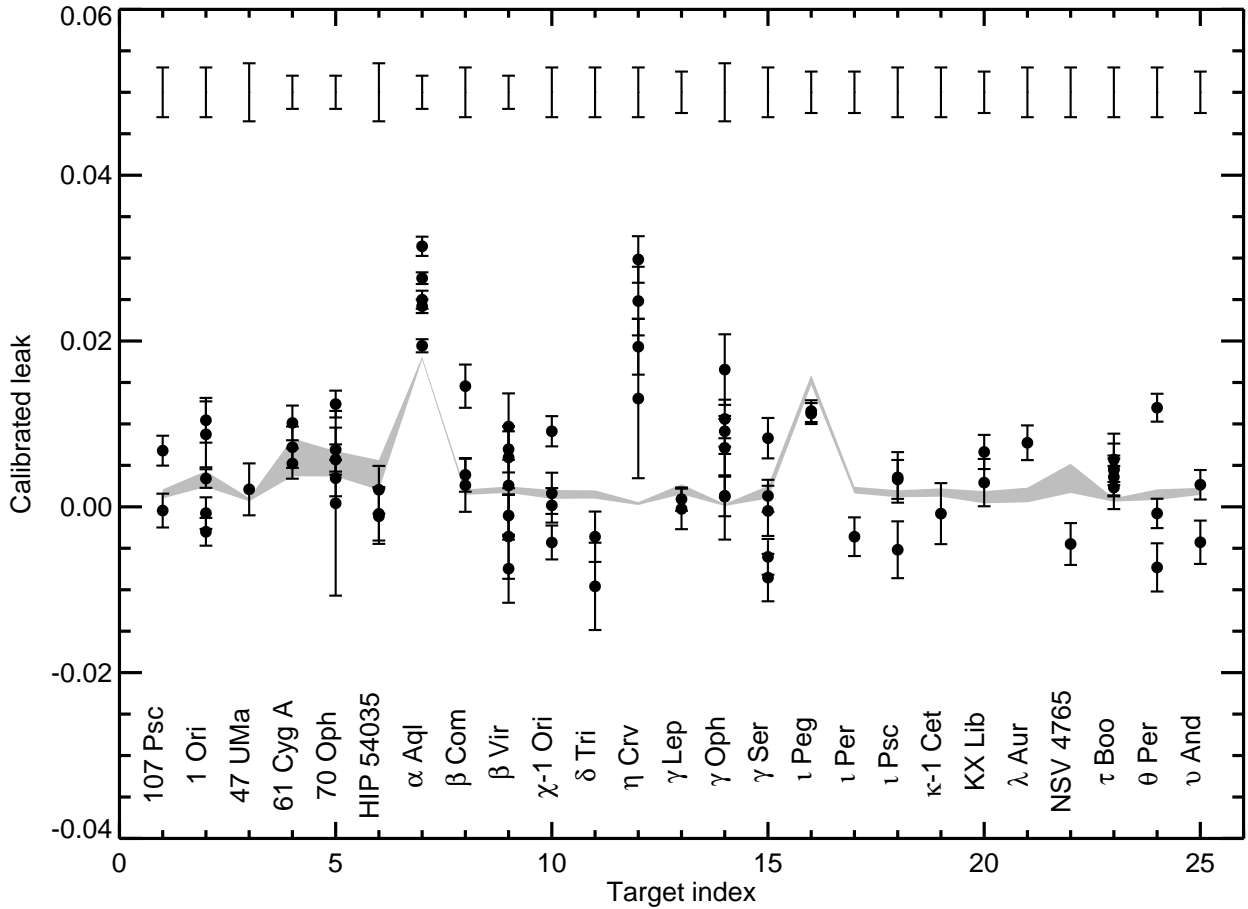


Fig. 3.— Calibrated data for the wideband  $8-9\ \mu\text{m}$  channel only. As in the previous figures, the external errors are shown as the bars at the top of the figure. The leak level due to the central stars, and its uncertainty, are also shown (grey band). We note that, as described in the text, at this stage in the analysis the multiple leak measurements for each target are not averaged, because they are allowed to vary with time as Earth rotation changes the baseline length and orientation.



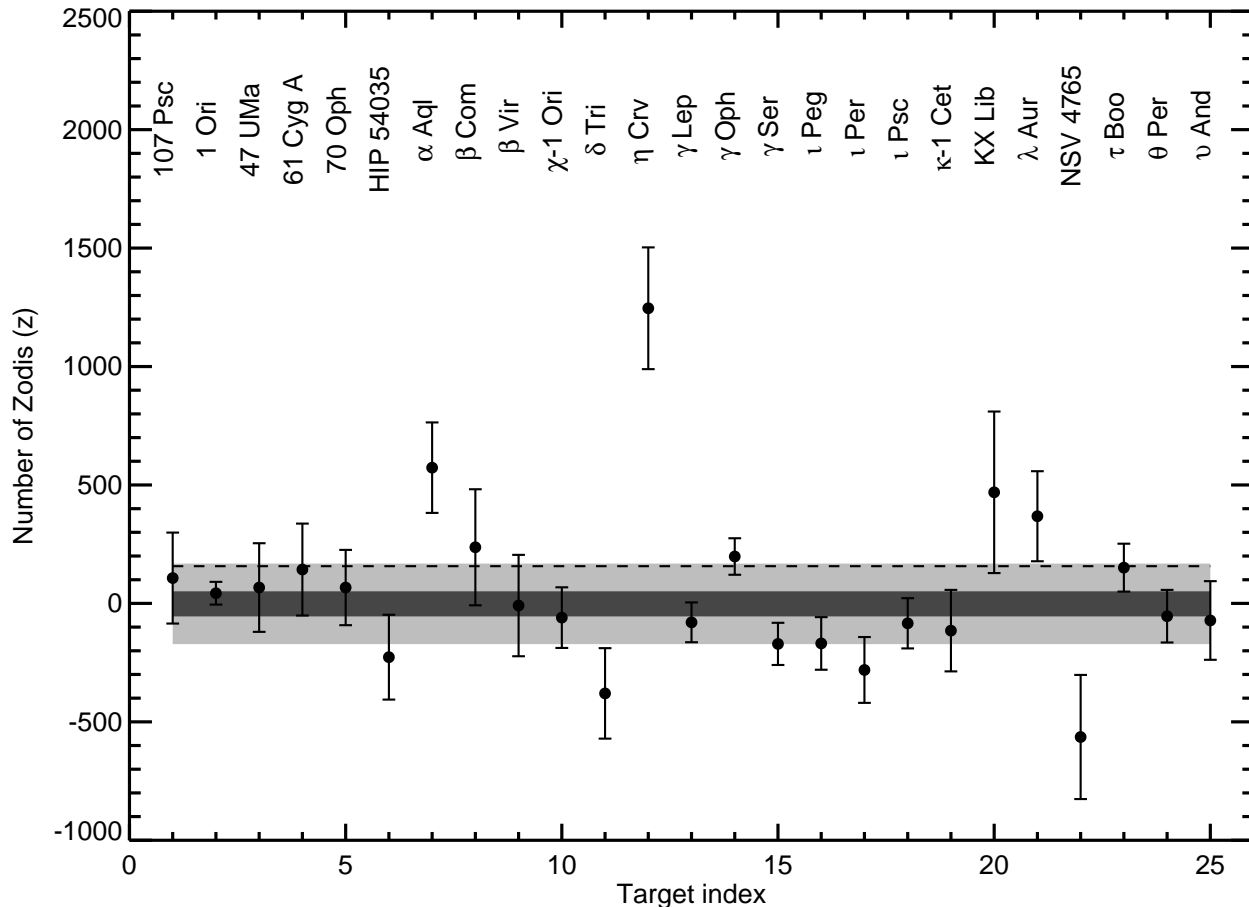


Fig. 4.— Average exozodi level per target. For the 22 clear non-detections, the weighted data scatter is 150 zodis, similar to typical measurement errors (mean 160 zodis), indicating that they have been accurately determined (see Section 5.4). For the sub-sample of 23 stars not previously known to have circumstellar dust (excludes  $\eta$  Crv and  $\gamma$  Oph) the mean is  $\hat{z} = +2$ , and the weighted scatter is  $\sigma = 170$  zodis. The light grey band covers the range  $\hat{z} \pm \sigma$ . As discussed in Section 6.2, under the assumption that these 23 stars are representative a class from the point of view of the exo-zodi emission, and if the individual measurements are uncorrelated, we measure a mean and error in the mean  $+2 \pm 50$  zodis, and this range is shown by the dark-grey band. The dashed line represents the  $3\sigma$  upper-limit (150 zodis) inferred for the mean exo-zodi level for the class.

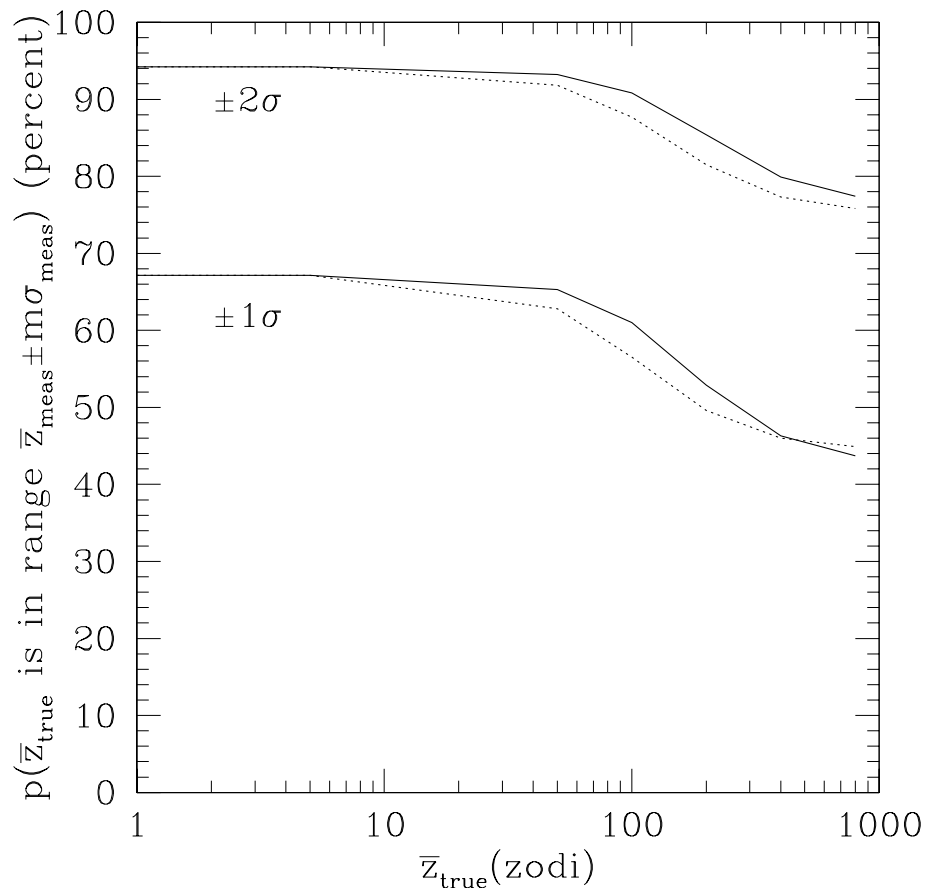


Fig. 5.— Probability that the true mean zodi level is in the range given by the simulated values of the mean plus or minus 1 (bottom curves) or 2 (top curves) times the error in the mean, assuming a uniform distribution of true zodi values (solid line) or a half-exponential distribution (dotted line).

Table 1. Target list.

Name	Spectral Type	RA	Dec	V	J	K	N	d (pc)	R <sub>*</sub> (R <sub>⊙</sub> )	L <sub>*</sub> (L <sub>⊙</sub> )	T <sub>*</sub> (K)	θ <sub>*</sub> (mas)	Age (Gyr)	R <sub>HZ</sub> (AU)	Comments
107 Psc	HIP7981	01:42:29.7	+20:16:06.6	5.2	3.8	3.3	1.6	7.47	0.81	0.428	5180	1.1 ± 0.2	2.9 – 13.0	0.85	Binary
1 Ori	HIP22449	04:49:50.4	+06:57:40.6	3.2	2.0	1.6	2.4	8.03	1.30	2.629	6450	1.5 ± 0.2	0.8 – 1.9	1.91	...
47 UMa	HIP53721	10:59:27.9	+40:25:48.9	5.1	4.0	3.7	1.3	14.1	1.22	1.555	5860	0.8 ± 0.1	4.2 – 5.9	1.54	3 RV planets
61 Cyg a	HIP104214	21:06:53.9	+38:44:57.9	5.2	3.1	2.2	5.5	3.48	0.74	0.167	4300	2.0 ± 0.4	...	0.57	Binary
70 Oph	HIP88601	18:05:27.3	+02:30:00.3	4.0	2.3	1.8	7.0	5.09	0.99	0.615	5140	2.2 ± 0.3	1.1 – 1.9	1.03	Binary
HD95735	HIP54035	11:03:20.2	+35:58:11.5	7.5	4.2	3.2	1.3	2.55	0.34	0.020	3730	1.7 ± 0.4	...	0.20	...
α Aql	HIP97649	19:50:47.0	+08:52:05.9	0.8	0.3	0.1	31.0	5.14	1.79	9.845	7650	3.1 ± 0.5	0.7	3.33	...
β Com	HIP64394	13:11:52.3	+27:52:41.4	4.3	3.2	2.9	2.4	9.15	1.09	1.341	5960	1.1 ± 0.1	0.5 – 3.0	1.42	...
β Vir	HIP57757	11:50:41.7	+01:45:52.9	3.6	2.6	2.3	4.3	10.90	1.68	3.443	6080	1.5 ± 0.1	2.3 – 3.4	2.26	...
χ1 Ori	HIP27913	05:54:22.9	+20:16:34.2	4.4	3.4	3.0	2.4	8.66	0.98	1.05	5930	1.1 ± 0.2	1.4 – 5.5	1.26	...
δ Tri	HIP10644	02:17:03.2	+34:13:27.2	4.9	3.5	3.1	1.8	10.85	1.02	1.09	5860	1.0 ± 0.2	1.9	1.29	...
η Crv	HIP61174	12:32:04.2	-16:11:45.6	4.3	3.6	3.4	1.8	18.21	1.53	4.679	6870	0.8 ± 0.2	0.95	2.46	High dust
γ Lep A	HIP27072	05:44:27.7	-22:26:54.1	3.6	2.7	2.4	3.8	8.97	1.22	2.259	6410	1.3 ± 0.2	1.3 – 2.5	1.78	...
γ Oph	HIP87108	17:47:53.5	+02:42:26.2	3.7	3.6	3.6	1.2	29.05	1.92	21.937	9030	0.5 ± 0.1	0.2	4.32	High dust
γ Ser	HIP78072	15:56:27.1	+15:39:41.8	3.8	3.1	2.7	2.3	11.12	1.37	2.741	6370	1.2 ± 0.3	3.4 – 3.9	1.97	...
ι Peg	HIP109176	22:07:00.6	+25:20:42.4	3.8	2.9	2.6	2.8	11.76	1.42	3.319	6540	1.1 ± 0.2	1.97	2.13	Binary
ι Per	HIP14632	03:09:04.0	+49:36:47.7	4.0	3.1	2.7	2.9	10.53	1.42	2.176	5890	1.2 ± 0.1	3.0 – 3.3	1.82	...
ι Psc	HIP116771	23:39:57.0	+05:37:34.6	4.1	3.3	2.9	2.3	13.79	1.57	3.324	6240	1.0 ± 0.1	3.5 – 4.0	2.19	...
κ1 Cet	HIP15457	03:19:21.6	+03:22:12.7	4.8	3.4	2.9	1.6	9.16	0.97	0.832	5620	1.1 ± 0.2	0.6 – 4.1	1.66	...
kx Lib	HIP73184	14:57:27.9	-21:24:55.7	5.7	3.7	3.0	3.4	5.91	0.82	0.263	4570	1.4 ± 0.5	0.2 – 11.6	0.70	Binary
λ Aur	HIP24813	05:19:08.4	+40:05:56.5	4.7	3.4	3.0	1.9	12.65	1.30	1.726	5820	1.0 ± 0.3	3.3 – 4.7	1.63	...
NSV4765	HIP49908	10:11:22.1	+49:27:15.2	6.6	3.9	2.9	1.9	4.87	0.79	0.133	3920	1.6 ± 0.4	4.7	0.52	...
τ Boo	HIP67275	13:47:15.7	+17:27:24.8	4.5	3.6	3.5	1.6	15.60	1.43	2.99	6370	0.8 ± 0.1	0.7 – 1.7	2.05	1 RV planet

Table 1—Continued

Name	Spectral Type	RA	Dec	V	J	K	N	d	R <sub>★</sub>	L <sub>★</sub>	T <sub>★</sub>	θ <sub>★</sub>	Age	R <sub>HZ</sub>	Comments	Age	Referen
							(Jy)	(pc)	(R <sub>☉</sub> )	(L <sub>☉</sub> )	(K)	(mas)	(Gyr)	(AU)			
<i>θ</i> Per	HIP12777	02:44:11.9	+49:13:42.4	4.1	3.0	2.7	2.0	11.23	1.24	2.188	6320	1.0 ± 0.2	0.5 – 2.0	1.77	...	...	1
<i>v</i> And	HIP7513	01:36:47.8	+41:24:19.6	4.1	3.2	2.9	2.6	13.47	1.62	3.301	6120	1.1 ± 0.1	2.3 – 3.0	2.20	3 RV planets		1

Note. —  $R_{\text{HZ}}$  is the radius of the center of the habitable zone. Stellar data from NStED. Diameters from NEoScl/fBol (validated with surface brightness relations). Age referen  
1: Valenti & Fischer (2005), 2: Wright et al. (2004), 3: Mamajek & Hillenbrand (2008), 4: Rieke et al. (2005), 5: Vizier online data catalog V/89 (Marsakov & Shevelev 1995)  
Holmberg et al. (2009), 7: Rhee et al. (2007), 8: Bryden et al. (2006)

Table 2. Calibrator Stars.

Name	Spectral Type	$\theta_*(K)$ (mas)	error (mas)	$\theta_*(N)$ (mas)	error (mas)	Calibrator for
HD1635	K3III	1.593	0.09	1.619	0.10	$\iota$ Psc
HD7106	K0III	1.871	0.10	1.901	0.11	$\delta$ Tri
HD7147	K4III	1.273	0.13	1.293	0.14	$\iota$ Psc
HD12594	K4III	1.578	0.15	1.603	0.15	107 Psc
HD13363	K4III	1.542	0.18	1.567	0.18	107 Psc
HD14770	G8III	1.226	0.21	1.245	0.21	$\theta$ Per
HD15779	G3III	1.569	0.30	1.594	0.31	$\kappa$ 1 Cet
HD16028	K4III	1.601	0.10	1.627	0.11	$\nu$ And
HD16160	K3V	1.138	0.31	1.156	0.31	$\kappa$ 1 Cet
HD18339	K3III	1.586	0.14	1.611	0.14	$\theta$ Per, $\iota$ Per
HD23413	K4III	1.875	0.18	1.905	0.18	1 Ori
HD29317	K0III	1.686	0.19	1.713	0.19	$\theta$ Per, $\iota$ Per
HD30557	G9III	1.116	0.16	1.134	0.17	$\lambda$ Aur
HD34559	G8III	1.091	0.33	1.108	0.34	$\chi$ 1 Ori
HD36780	K5III	2.017	0.12	2.049	0.12	1 Ori
HD36923	M0III	1.462	0.13	1.486	0.13	$\gamma$ Lep
HD42341	K2III	1.141	0.10	1.159	0.10	$\gamma$ Lep
HD42398	K0III	1.027	0.20	1.043	0.20	$\chi$ 1 Ori
HD43993	K1III	1.484	0.10	1.507	0.10	$\gamma$ Lep
HD45433	K5III	1.818	0.22	1.847	0.22	1 Ori
HD46374	K2III	1.363	0.19	1.385	0.19	$\chi$ 1 Ori
HD46709	K4III	1.700	0.09	1.727	0.09	$\chi$ 1 Ori
HD47070	K5III	1.255	0.23	1.275	0.23	$\lambda$ Aur
HD93859	K2III	0.950	0.22	0.965	0.22	NSV4765
HD94669	K2III	1.098	0.15	1.115	0.15	47 Uma, HD95735
HD95345	K1III	2.077	0.15	2.111	0.16	$\beta$ Vir
HD95849	K3III	0.614	0.70	0.623	0.71	$\eta$ Crv
HD99967	K2III	1.124	0.14	1.142	0.14	47 Uma, HD95735, NSV4765
HD100343	K4III	1.432	0.15	1.455	0.15	$\eta$ Crv
HD102159	M4III	4.232	0.09	4.299	0.09	HD95735
HD103500	M3III	2.526	0.18	2.566	0.18	HD95735

Table 2—Continued

Name	Spectral Type	$\theta_*(K)$ (mas)	error (mas)	$\theta_*(N)$ (mas)	error (mas)	Calibrator for
HD104979	G8III	1.981	0.09	2.012	0.09	$\beta$ Vir
HD107325	K2III	1.088	0.25	1.105	0.26	$\beta$ Com
HD107328	K1III	1.904	0.14	1.934	0.14	$\beta$ Vir
HD107418	K0III	1.098	0.26	1.116	0.27	$\eta$ Crv
HD109317	K0III	1.062	0.06	1.079	0.06	$\beta$ Com
HD117818	K0III	0.931	0.39	0.946	0.40	$\eta$ Crv
HD118840	M3III	1.241	0.12	1.261	0.12	$\tau$ Boo
HD119126	G9III	1.005	0.16	1.021	0.16	$\beta$ Com
HD119584	K4III	1.595	0.10	1.620	0.10	$\tau$ Boo
HD124206	K2III	1.958	0.23	1.989	0.24	kx Lib
HD129972	K0III	1.526	0.23	1.551	0.24	$\gamma$ Ser
HD144889	K4III	1.266	0.11	1.286	0.11	$\tau$ Boo
HD147547	A9III	0.907	0.13	0.921	0.13	$\gamma$ Ser
HD151217	K5III	3.187	0.22	3.238	0.23	70 Oph
HD152601	K2III	0.998	0.23	1.014	0.23	$\gamma$ Oph
HD166460	K2III	1.062	0.14	1.079	0.14	$\gamma$ Oph
HD170474	K0III	0.886	0.15	0.900	0.16	$\gamma$ Oph
HD171391	G8III	1.076	0.14	1.093	0.15	$\gamma$ Oph
HD176678	K1III	2.867	0.18	2.913	0.18	70 Oph
HD184406	K3III	3.001	0.07	3.049	0.07	70 Oph, $\alpha$ Aql
HD198134	K3III	2.053	0.25	2.085	0.25	$\iota$ Peg
HD199169	K4III	2.715	0.17	2.759	0.17	$\iota$ Peg
HD205512	K1III	2.028	0.24	2.060	0.24	61 Cyg a
HD213119	K5III	2.332	0.08	2.369	0.08	$\iota$ Psc
HD217459	K4III	1.326	0.10	1.347	0.10	$\iota$ Psc

Note. — Calibrator uniform disk angular diameters ( $\theta_*$ , at K and N-band) are from Appendix A of Colavita et al. (2009).

Table 3. Log of Observations and Calibrated Leak Data (wideband channel 8 – 9  $\mu\text{m}$ ).

Name	Date	HA	u (m)	v (m)	$L_{calibrated}$	$\sigma_{L_{calibrated}}^{formal}$	$\sigma_{L_{calibrated}}^{ext.}$	$L_{\star}$
107 Psc	UT 2008 Oct 13	2.54	26.5162	76.8456	0.006772	0.001803	0.003000	0.001605 $\pm$ 0.000554
107 Psc	UT 2008 Oct 13	3.27	16.6299	78.2699	-0.000451	0.002041	0.003000	0.001555 $\pm$ 0.000537
1 Ori	UT 2008 Feb 17	0.41	48.9782	69.3127	-0.003011	0.001677	0.003000	0.003428 $\pm$ 0.000979
1 Ori	UT 2008 Feb 17	1.10	43.0509	72.2259	0.003409	0.001118	0.003000	0.003365 $\pm$ 0.000961
1 Ori	UT 2008 Feb 17	1.83	35.3784	74.8085	-0.000761	0.001905	0.003000	0.003259 $\pm$ 0.000931
1 Ori	UT 2008 Feb 18	0.10	51.1001	67.9093	0.010442	0.002699	0.003000	0.003438 $\pm$ 0.000982
1 Ori	UT 2008 Feb 18	1.22	41.8864	72.6852	0.008744	0.003977	0.003000	0.003349 $\pm$ 0.000957
47 UMa	UT 2009 Jan 10	-1.08	56.0337	53.2305	0.002110	0.003131	0.003500	0.000846 $\pm$ 0.000201
61 Cyg A	UT 2008 Aug 17	0.46	48.5433	67.6194	0.010119	0.002093	0.002000	0.005730 $\pm$ 0.002202
61 Cyg A	UT 2008 Aug 17	1.12	42.8783	72.5475	0.005219	0.001828	0.002000	0.005873 $\pm$ 0.002257
61 Cyg A	UT 2008 Aug 17	1.70	36.7988	76.3515	0.007192	0.002493	0.002000	0.005941 $\pm$ 0.002283
70 Oph	UT 2008 Aug 17	1.27	41.3929	65.0748	0.012394	0.001618	0.002000	0.005621 $\pm$ 0.001658
70 Oph	UT 2008 Aug 17	1.86	34.9364	65.3338	0.005707	0.001824	0.002000	0.005187 $\pm$ 0.001530
70 Oph	UT 2008 Aug 18	0.35	49.3793	64.5963	0.003461	0.002184	0.002000	0.006247 $\pm$ 0.001842
70 Oph	UT 2008 Aug 18	1.03	43.6993	64.9598	0.000431	0.011140	0.002000	0.005792 $\pm$ 0.001708
70 Oph	UT 2008 Aug 18	1.89	34.6930	65.3421	0.006900	0.002653	0.002000	0.005172 $\pm$ 0.001525
HIP 54035	UT 2008 Apr 14	2.75	23.7420	81.4917	-0.000848	0.003220	0.003500	0.003984 $\pm$ 0.001872
HIP 54035	UT 2008 Apr 14	3.45	14.0496	83.5171	-0.001139	0.003330	0.003500	0.003966 $\pm$ 0.001864
HIP 54035	UT 2009 Jan 10	-0.23	53.0053	62.9383	0.002060	0.002876	0.003500	0.003744 $\pm$ 0.001759
$\alpha$ Aql	UT 2008 May 25	-1.22	56.2663	63.5521	0.027578	0.000705	0.002000	0.018738 $\pm$ 0.000167
$\alpha$ Aql	UT 2008 May 25	-0.42	53.9181	65.3231	0.024192	0.000818	0.002000	0.018658 $\pm$ 0.000166
$\alpha$ Aql	UT 2008 May 26	-0.93	55.6966	64.1969	0.024979	0.001091	0.002000	0.018786 $\pm$ 0.000167
$\alpha$ Aql	UT 2008 May 26	-0.25	53.0955	65.6963	0.031427	0.001162	0.002000	0.018557 $\pm$ 0.000165
$\alpha$ Aql	UT 2008 May 26	0.35	49.4061	66.9415	0.019427	0.000794	0.002000	0.018003 $\pm$ 0.000160
$\beta$ Com	UT 2008 Feb 16	0.20	50.4131	68.0667	0.014552	0.002608	0.003000	0.001774 $\pm$ 0.000320
$\beta$ Com	UT 2008 Feb 16	1.08	43.2738	73.1044	0.002594	0.003199	0.003000	0.001784 $\pm$ 0.000322
$\beta$ Com	UT 2008 Feb 16	1.87	34.8345	76.9074	0.003855	0.002029	0.003000	0.001762 $\pm$ 0.000318
$\beta$ Vir	UT 2008 Feb 17	1.66	37.2863	64.7000	-0.001053	0.002496	0.002000	0.002551 $\pm$ 0.000473
$\beta$ Vir	UT 2008 Feb 17	2.33	29.2457	64.8762	0.006946	0.002802	0.002000	0.002317 $\pm$ 0.000430
$\beta$ Vir	UT 2008 Feb 17	3.04	19.8380	65.0126	0.009681	0.004003	0.002000	0.002114 $\pm$ 0.000392
$\beta$ Vir	UT 2008 Feb 18	1.55	38.4409	64.6688	-0.003591	0.005091	0.002000	0.002590 $\pm$ 0.000480

Table 3—Continued

Name	Date	HA	u (m)	v (m)	$L_{calibrated}$	$\sigma_{L_{calibrated}}^{formal}$	$\sigma_{L_{calibrated}}^{ext.}$	$L_{\star}$
$\beta$ Vir	UT 2008 Feb 18	2.56	26.3314	64.9254	-0.007462	0.004110	0.002000	$0.002246 \pm 0.000416$
$\beta$ Vir	UT 2008 Feb 18	2.69	24.5754	64.9519	0.002577	0.006531	0.002000	$0.002207 \pm 0.000409$
$\beta$ Vir	UT 2008 Feb 18	3.25	16.8910	65.0429	0.005953	0.003708	0.002000	$0.002066 \pm 0.000383$
$\chi$ -1 Ori	UT 2009 Jan 10	1.15	42.5623	72.4220	0.009114	0.001823	0.003000	$0.001621 \pm 0.000576$
$\chi$ -1 Ori	UT 2009 Jan 10	1.90	34.5281	75.0401	0.000176	0.002080	0.003000	$0.001568 \pm 0.000557$
$\chi$ -1 Ori	UT 2009 Jan 13	2.35	29.0718	76.3297	0.001628	0.002485	0.003000	$0.001533 \pm 0.000544$
$\chi$ -1 Ori	UT 2009 Jan 13	3.35	15.5151	78.3664	-0.004302	0.002044	0.003000	$0.001466 \pm 0.000521$
$\delta$ Tri	UT 2008 Nov 13	0.44	48.7305	68.5848	-0.009594	0.005263	0.003000	$0.001449 \pm 0.000488$
$\delta$ Tri	UT 2008 Nov 13	1.95	33.9310	77.9062	-0.003606	0.003037	0.003000	$0.001478 \pm 0.000498$
$\eta$ Crv	UT 2008 Apr 17	-1.93	56.3123	62.3397	0.024819	0.004139	0.003000	$0.000976 \pm 0.000423$
$\eta$ Crv	UT 2008 May 24	0.71	46.6175	51.9715	0.029837	0.002808	0.003000	$0.000674 \pm 0.000292$
$\eta$ Crv	UT 2008 May 24	1.91	34.3913	48.3670	0.019313	0.003375	0.003000	$0.000487 \pm 0.000211$
$\eta$ Crv	UT 2008 May 24	2.61	25.6853	46.8307	0.013058	0.009607	0.003000	$0.000394 \pm 0.000171$
$\gamma$ Lep	UT 2009 Jan 10	-0.96	55.7760	55.1121	-0.000252	0.002443	0.002500	$0.001990 \pm 0.000564$
$\gamma$ Lep	UT 2009 Jan 13	-1.25	56.3146	56.7235	0.000925	0.001408	0.002500	$0.002068 \pm 0.000586$
$\gamma$ Oph	UT 2008 Jul 16	-1.09	56.0575	63.7328	0.016556	0.004257	0.003500	$0.000306 \pm 0.000173$
$\gamma$ Oph	UT 2008 Jul 16	0.93	44.6871	65.0191	0.007115	0.003479	0.003500	$0.000264 \pm 0.000149$
$\gamma$ Oph	UT 2008 Jul 16	2.18	31.1048	65.6124	0.009111	0.001849	0.003500	$0.000224 \pm 0.000127$
$\gamma$ Oph	UT 2008 Jul 17	-1.20	56.2478	63.6559	0.001213	0.005165	0.003500	$0.000306 \pm 0.000173$
$\gamma$ Oph	UT 2008 Jul 17	1.12	42.8833	65.1234	0.001334	0.002470	0.003500	$0.000258 \pm 0.000146$
$\gamma$ Oph	UT 2008 Jul 17	2.20	30.9258	65.6180	0.010596	0.002324	0.003500	$0.000223 \pm 0.000126$
$\gamma$ Ser	UT 2008 Apr 16	0.73	46.4220	69.8053	0.001319	0.001941	0.003000	$0.002031 \pm 0.000880$
$\gamma$ Ser	UT 2008 Apr 16	1.46	39.4365	72.0252	0.008282	0.002438	0.003000	$0.001948 \pm 0.000844$
$\gamma$ Ser	UT 2008 Apr 16	2.62	25.5293	74.7012	-0.000487	0.003023	0.003000	$0.001801 \pm 0.000780$
$\gamma$ Ser	UT 2008 Apr 17	2.40	28.4275	74.2770	-0.006036	0.002157	0.003000	$0.001828 \pm 0.000792$
$\gamma$ Ser	UT 2008 Apr 17	2.93	21.3939	75.2099	-0.008536	0.002857	0.003000	$0.001767 \pm 0.000766$
$\iota$ Peg	UT 2008 Jul 14	1.27	41.3608	73.8551	0.011249	0.001265	0.002500	$0.015200 \pm 0.000590$
$\iota$ Peg	UT 2008 Jul 14	1.98	33.5176	76.8496	0.011541	0.001314	0.002500	$0.015300 \pm 0.000579$
$\iota$ Per	UT 2009 Jan 11	1.34	40.6795	71.0095	-0.003608	0.002332	0.002500	$0.001968 \pm 0.000390$
$\iota$ Psc	UT 2008 Aug 18	-0.46	54.0668	64.7804	-0.005178	0.003428	0.003000	$0.001545 \pm 0.000416$
$\iota$ Psc	UT 2008 Oct 13	-1.79	56.4656	62.8581	0.003308	0.002344	0.003000	$0.001550 \pm 0.000417$



Table 3—Continued

Name	Date	HA	u (m)	v (m)	$L_{calibrated}$	$\sigma_{L_{calibrated}}^{formal}$	$\sigma_{L_{calibrated}}^{ext.}$	$L_{\star}$
$\iota$ Psc	UT 2008 Oct 13	-0.93	55.7001	64.1049	0.003550	0.003045	0.003000	$0.001565 \pm 0.000421$
$\kappa$ -1 Cet	UT 2009 Jan 10	-0.13	52.4351	64.5998	-0.000822	0.003682	0.003000	$0.001681 \pm 0.000489$
KX Lib	UT 2008 May 26	1.25	41.6389	45.0668	0.006615	0.002061	0.002500	$0.001588 \pm 0.001008$
KX Lib	UT 2008 May 26	2.14	31.5908	41.9053	0.002920	0.002855	0.002500	$0.001162 \pm 0.000737$
$\lambda$ Aur	UT 2009 Jan 12	0.62	47.3438	68.4446	0.007726	0.002093	0.003000	$0.001390 \pm 0.000862$
NSV 4765	UT 2009 Jan 10	1.90	34.5687	75.2646	-0.004485	0.002523	0.003000	$0.003350 \pm 0.001718$
$\tau$ Boo	UT 2008 May 25	1.40	40.1023	72.4754	0.004442	0.003189	0.003000	$0.000903 \pm 0.000223$
$\tau$ Boo	UT 2008 May 25	2.28	29.8482	74.9182	0.005715	0.003108	0.003000	$0.000856 \pm 0.000211$
$\tau$ Boo	UT 2008 May 25	3.05	19.6580	76.4125	0.002326	0.002604	0.003000	$0.000820 \pm 0.000202$
$\tau$ Boo	UT 2008 May 27	1.84	35.2712	73.7720	0.004587	0.001592	0.003000	$0.000880 \pm 0.000217$
$\tau$ Boo	UT 2008 May 27	2.76	23.6261	75.9201	0.003603	0.002224	0.003000	$0.000832 \pm 0.000206$
$\theta$ Per	UT 2009 Jan 11	0.49	48.3812	63.5750	0.011956	0.001680	0.003000	$0.001333 \pm 0.000575$
$\theta$ Per	UT 2009 Jan 11	2.32	29.3767	78.0123	-0.007308	0.002905	0.003000	$0.001451 \pm 0.000626$
$\theta$ Per	UT 2009 Jan 12	1.93	34.1275	75.5641	-0.000798	0.001769	0.003000	$0.001435 \pm 0.000619$
$\nu$ And	UT 2008 Nov 12	2.53	26.6782	80.5610	-0.004274	0.002613	0.002500	$0.001845 \pm 0.000425$
$\nu$ And	UT 2008 Nov 12	3.43	14.2844	83.7755	0.002662	0.001777	0.002500	$0.001851 \pm 0.000426$

Note. — Table 3 is published in its entirety in the electronic edition of the *Astrophysical Journal*. A portion is shown here for guidance regarding its form and content.

Table 4. Number of zodis for each observation and each zodi disk orientation.

Name	Date	HA	$i_{disk}$ ( $^{\circ}$ )	$PA_{disk}$ ( $^{\circ}$ )	$z_{ij}$	$\sigma_{ij}^{formal}$	$\sigma_j^{ext}$	$\sigma^*$	$R_{half-light}$ (AU)
107 Psc	UT 2008 Oct 13	2.54	0.0	109.0	256	88	147	27	0.07
107 Psc	UT 2008 Oct 13	2.54	90.0	109.0	358	123	205	38	0.07
107 Psc	UT 2008 Oct 13	2.54	90.0	19.0	244	84	141	26	0.06
107 Psc	UT 2008 Oct 13	3.27	0.0	102.0	-98	100	148	26	0.07
107 Psc	UT 2008 Oct 13	3.27	90.0	102.0	-135	137	202	36	0.07
107 Psc	UT 2008 Oct 13	3.27	90.0	12.0	-95	97	142	25	0.06
1 Ori	UT 2008 Feb 17	0.41	0.0	125.2	-143	37	67	21	0.10
1 Ori	UT 2008 Feb 17	0.41	90.0	125.2	-180	47	84	27	0.10
1 Ori	UT 2008 Feb 17	0.41	90.0	35.2	-113	29	53	17	0.08
1 Ori	UT 2008 Feb 17	1.10	0.0	120.8	1	25	67	21	0.10
1 Ori	UT 2008 Feb 17	1.10	90.0	120.8	1	31	83	26	0.10
1 Ori	UT 2008 Feb 17	1.10	90.0	30.8	0	20	53	17	0.08
1 Ori	UT 2008 Feb 17	1.83	0.0	115.3	-90	42	67	20	0.10
1 Ori	UT 2008 Feb 17	1.83	90.0	115.3	-105	50	78	24	0.10
1 Ori	UT 2008 Feb 17	1.83	90.0	25.3	-76	36	57	17	0.08
1 Ori	UT 2008 Feb 18	0.10	0.0	127.0	158	60	67	22	0.10
1 Ori	UT 2008 Feb 18	0.10	90.0	127.0	189	71	79	26	0.10
1 Ori	UT 2008 Feb 18	0.10	90.0	37.0	132	50	56	18	0.08
1 Ori	UT 2008 Feb 18	1.22	0.0	120.0	121	89	67	21	0.10
1 Ori	UT 2008 Feb 18	1.22	90.0	120.0	150	109	82	26	0.10
1 Ori	UT 2008 Feb 18	1.22	90.0	30.0	98	72	54	17	0.08
47 UMa	UT 2009 Jan 10	-1.08	0.0	136.5	62	154	172	9	0.14
47 UMa	UT 2009 Jan 10	-1.08	90.0	136.5	84	208	233	13	0.14
47 UMa	UT 2009 Jan 10	-1.08	90.0	46.5	61	151	169	9	0.11
61 Cyg A	UT 2008 Aug 17	0.46	0.0	125.7	367	173	165	184	-0.01
61 Cyg A	UT 2008 Aug 17	0.46	90.0	125.7	507	237	226	254	0.03
61 Cyg A	UT 2008 Aug 17	0.46	90.0	35.7	324	153	146	162	0.03
61 Cyg A	UT 2008 Aug 17	1.12	0.0	120.6	-54	151	165	187	0.03
61 Cyg A	UT 2008 Aug 17	1.12	90.0	120.6	-75	210	229	261	0.03
61 Cyg A	UT 2008 Aug 17	1.12	90.0	30.6	-47	131	143	163	0.03
61 Cyg A	UT 2008 Aug 17	1.70	0.0	115.7	104	206	165	190	0.03

Table 4—Continued

Name	Date	HA	$i_{disk}$ ( $^{\circ}$ )	$PA_{disk}$ ( $^{\circ}$ )	$z_{ij}$	$\sigma_{ij}^{formal}$	$\sigma_j^{ext}$	$\sigma^*$	$R_{half-light}$ (AU)
61 Cyg A	UT 2008 Aug 17	1.70	90.0	115.7	143	282	226	262	0.03
61 Cyg A	UT 2008 Aug 17	1.70	90.0	25.7	91	180	144	166	0.03
70 Oph	UT 2008 Aug 17	1.27	0.0	122.5	551	129	160	134	0.06
70 Oph	UT 2008 Aug 17	1.27	90.0	122.5	755	176	218	184	0.06
70 Oph	UT 2008 Aug 17	1.27	90.0	32.5	461	108	134	113	0.05
70 Oph	UT 2008 Aug 17	1.86	0.0	118.1	42	147	161	124	0.06
70 Oph	UT 2008 Aug 17	1.86	90.0	118.1	56	195	214	165	0.06
70 Oph	UT 2008 Aug 17	1.86	90.0	28.1	36	126	139	107	0.05
70 Oph	UT 2008 Aug 18	0.35	0.0	127.4	-223	174	159	147	0.06
70 Oph	UT 2008 Aug 18	0.35	90.0	127.4	-294	229	210	194	0.06
70 Oph	UT 2008 Aug 18	0.35	90.0	37.4	-190	148	136	126	-0.01
70 Oph	UT 2008 Aug 18	1.03	0.0	123.9	-430	893	160	137	0.06
70 Oph	UT 2008 Aug 18	1.03	90.0	123.9	-585	1216	218	186	0.06
70 Oph	UT 2008 Aug 18	1.03	90.0	33.9	-358	743	133	114	0.05
70 Oph	UT 2008 Aug 18	1.89	0.0	118.0	140	214	161	123	0.06
70 Oph	UT 2008 Aug 18	1.89	90.0	118.0	187	284	214	165	0.06
70 Oph	UT 2008 Aug 18	1.89	90.0	28.0	121	184	139	106	0.05
HIP 54035	UT 2008 Apr 14	2.75	0.0	106.2	-286	191	207	110	0.02
HIP 54035	UT 2008 Apr 14	2.75	90.0	106.2	-456	305	331	176	0.02
HIP 54035	UT 2008 Apr 14	2.75	90.0	16.2	-276	184	200	106	-0.01
HIP 54035	UT 2008 Apr 14	3.45	0.0	99.5	-302	197	207	110	0.02
HIP 54035	UT 2008 Apr 14	3.45	90.0	99.5	-473	309	325	172	-0.01
HIP 54035	UT 2008 Apr 14	3.45	90.0	9.5	-293	191	201	107	-0.01
HIP 54035	UT 2009 Jan 10	-0.23	0.0	130.1	-101	172	210	105	-0.01
HIP 54035	UT 2009 Jan 10	-0.23	90.0	130.1	-164	278	338	171	0.02
HIP 54035	UT 2009 Jan 10	-0.23	90.0	40.1	-98	168	204	103	-0.01
$\alpha$ Aql	UT 2008 May 25	-1.22	0.0	131.5	828	64	182	15	0.17
$\alpha$ Aql	UT 2008 May 25	-1.22	90.0	131.5	462	35	101	8	0.11
$\alpha$ Aql	UT 2008 May 25	-1.22	90.0	41.5	766	59	168	14	0.08
$\alpha$ Aql	UT 2008 May 25	-0.42	0.0	129.5	517	74	182	15	0.17
$\alpha$ Aql	UT 2008 May 25	-0.42	90.0	129.5	312	45	109	9	0.11

Table 4—Continued

Name	Date	HA	$i_{disk}$ (°)	$PA_{disk}$ (°)	$z_{ij}$	$\sigma_{ij}^{formal}$	$\sigma_j^{ext}$	$\sigma^*$	$R_{half-light}$ (AU)
$\alpha$ Aql	UT 2008 May 25	-0.42	90.0	39.5	449	64	158	13	0.08
$\alpha$ Aql	UT 2008 May 26	-0.93	0.0	130.9	579	99	182	15	0.17
$\alpha$ Aql	UT 2008 May 26	-0.93	90.0	130.9	319	54	100	8	0.11
$\alpha$ Aql	UT 2008 May 26	-0.93	90.0	40.9	539	92	169	14	0.08
$\alpha$ Aql	UT 2008 May 26	-0.25	0.0	128.9	1211	105	182	15	0.17
$\alpha$ Aql	UT 2008 May 26	-0.25	90.0	128.9	809	70	121	10	0.10
$\alpha$ Aql	UT 2008 May 26	-0.25	90.0	38.9	971	84	146	12	0.09
$\alpha$ Aql	UT 2008 May 26	0.35	0.0	126.4	132	72	182	14	0.17
$\alpha$ Aql	UT 2008 May 26	0.35	90.0	126.4	128	69	175	14	0.10
$\alpha$ Aql	UT 2008 May 26	0.35	90.0	36.4	72	39	99	8	0.09
$\beta$ Com	UT 2008 Feb 16	0.20	0.0	126.5	568	114	131	14	-0.02
$\beta$ Com	UT 2008 Feb 16	0.20	90.0	126.5	783	155	179	19	0.09
$\beta$ Com	UT 2008 Feb 16	0.20	90.0	36.5	496	99	114	12	0.07
$\beta$ Com	UT 2008 Feb 16	1.08	0.0	120.6	35	140	131	14	0.09
$\beta$ Com	UT 2008 Feb 16	1.08	90.0	120.6	48	189	177	19	0.09
$\beta$ Com	UT 2008 Feb 16	1.08	90.0	30.6	31	123	115	12	0.07
$\beta$ Com	UT 2008 Feb 16	1.87	0.0	114.4	92	88	131	13	0.09
$\beta$ Com	UT 2008 Feb 16	1.87	90.0	114.4	120	116	171	18	0.09
$\beta$ Com	UT 2008 Feb 16	1.87	90.0	24.4	83	80	118	12	0.07
$\beta$ Vir	UT 2008 Feb 17	1.66	0.0	120.0	-201	139	111	26	0.13
$\beta$ Vir	UT 2008 Feb 17	1.66	90.0	120.0	-264	183	147	34	0.13
$\beta$ Vir	UT 2008 Feb 17	1.66	90.0	30.0	-168	116	93	22	0.11
$\beta$ Vir	UT 2008 Feb 17	2.33	0.0	114.3	261	157	112	24	0.15
$\beta$ Vir	UT 2008 Feb 17	2.33	90.0	114.3	335	200	143	31	0.14
$\beta$ Vir	UT 2008 Feb 17	2.33	90.0	24.3	227	136	97	21	0.11
$\beta$ Vir	UT 2008 Feb 17	3.04	0.0	107.0	431	226	112	22	0.15
$\beta$ Vir	UT 2008 Feb 17	3.04	90.0	107.0	532	276	138	27	0.14
$\beta$ Vir	UT 2008 Feb 17	3.04	90.0	17.0	390	204	102	20	0.11
$\beta$ Vir	UT 2008 Feb 18	1.55	0.0	120.7	-343	284	111	26	0.13
$\beta$ Vir	UT 2008 Feb 18	1.55	90.0	120.7	-453	376	147	35	0.13
$\beta$ Vir	UT 2008 Feb 18	1.55	90.0	30.7	-286	236	93	22	0.11

Table 4—Continued

Name	Date	HA	$i_{disk}$ ( $^{\circ}$ )	$PA_{disk}$ ( $^{\circ}$ )	$z_{ij}$	$\sigma_{ij}^{formal}$	$\sigma_j^{ext}$	$\sigma^*$	$R_{half-light}$ (AU)
$\beta$ Vir	UT 2008 Feb 18	2.56	0.0	112.1	-542	231	112	23	0.15
$\beta$ Vir	UT 2008 Feb 18	2.56	90.0	112.1	-678	291	141	29	0.14
$\beta$ Vir	UT 2008 Feb 18	2.56	90.0	22.1	-477	203	99	20	0.11
$\beta$ Vir	UT 2008 Feb 18	2.69	0.0	110.7	20	367	112	23	0.15
$\beta$ Vir	UT 2008 Feb 18	2.69	90.0	110.7	26	459	140	28	0.14
$\beta$ Vir	UT 2008 Feb 18	2.69	90.0	20.7	18	326	100	20	0.11
$\beta$ Vir	UT 2008 Feb 18	3.25	0.0	104.6	221	209	113	21	0.15
$\beta$ Vir	UT 2008 Feb 18	3.25	90.0	104.6	268	253	136	26	0.15
$\beta$ Vir	UT 2008 Feb 18	3.25	90.0	14.6	201	191	103	19	0.11
$\chi$ -1 Ori	UT 2009 Jan 10	1.15	0.0	120.4	368	88	146	28	0.09
$\chi$ -1 Ori	UT 2009 Jan 10	1.15	90.0	120.4	483	115	190	37	0.09
$\chi$ -1 Ori	UT 2009 Jan 10	1.15	90.0	30.4	337	81	133	25	0.07
$\chi$ -1 Ori	UT 2009 Jan 10	1.90	0.0	114.7	-67	101	146	27	0.09
$\chi$ -1 Ori	UT 2009 Jan 10	1.90	90.0	114.7	-87	130	188	34	0.09
$\chi$ -1 Ori	UT 2009 Jan 10	1.90	90.0	24.7	-62	94	135	25	0.07
$\chi$ -1 Ori	UT 2009 Jan 13	2.35	0.0	110.9	4	121	146	26	-0.02
$\chi$ -1 Ori	UT 2009 Jan 13	2.35	90.0	110.9	5	154	186	33	0.09
$\chi$ -1 Ori	UT 2009 Jan 13	2.35	90.0	20.9	4	113	136	24	0.07
$\chi$ -1 Ori	UT 2009 Jan 13	3.35	0.0	101.2	-281	100	146	25	-0.02
$\chi$ -1 Ori	UT 2009 Jan 13	3.35	90.0	101.2	-348	124	182	31	0.09
$\chi$ -1 Ori	UT 2009 Jan 13	3.35	90.0	11.2	-267	95	139	24	-0.02
$\delta$ Tri	UT 2008 Nov 13	0.44	0.0	125.4	-589	283	161	26	0.11
$\delta$ Tri	UT 2008 Nov 13	0.44	90.0	125.4	-840	408	232	37	0.11
$\delta$ Tri	UT 2008 Nov 13	0.44	90.0	35.4	-531	256	146	23	0.09
$\delta$ Tri	UT 2008 Nov 13	1.95	0.0	113.5	-272	163	161	26	0.11
$\delta$ Tri	UT 2008 Nov 13	1.95	90.0	113.5	-381	229	226	37	0.11
$\delta$ Tri	UT 2008 Nov 13	1.95	90.0	23.5	-249	149	147	24	0.09
$\eta$ Crv	UT 2008 Apr 17	-1.93	0.0	132.1	1145	193	140	20	-0.04
$\eta$ Crv	UT 2008 Apr 17	-1.93	90.0	132.1	1378	228	165	24	0.20
$\eta$ Crv	UT 2008 Apr 17	-1.93	90.0	42.1	1121	189	137	19	0.15
$\eta$ Crv	UT 2008 May 24	0.71	0.0	131.9	1446	134	144	14	0.22

Table 4—Continued

Name	Date	HA	$i_{disk}$ ( $^{\circ}$ )	$PA_{disk}$ ( $^{\circ}$ )	$z_{ij}$	$\sigma_{ij}^{formal}$	$\sigma_j^{ext}$	$\sigma^*$	$R_{\text{half-light}}$ (AU)
$\eta$ Crv	UT 2008 May 24	0.71	90.0	131.9	2131	192	205	21	0.22
$\eta$ Crv	UT 2008 May 24	0.71	90.0	41.9	1284	119	127	12	0.18
$\eta$ Crv	UT 2008 May 24	1.91	0.0	125.4	950	166	148	10	0.25
$\eta$ Crv	UT 2008 May 24	1.91	90.0	125.4	1516	259	230	17	0.25
$\eta$ Crv	UT 2008 May 24	1.91	90.0	35.4	818	143	127	9	0.18
$\eta$ Crv	UT 2008 May 24	2.61	0.0	118.7	648	484	151	8	0.27
$\eta$ Crv	UT 2008 May 24	2.61	90.0	118.7	1050	770	240	14	0.25
$\eta$ Crv	UT 2008 May 24	2.61	90.0	28.7	564	421	131	7	0.22
$\gamma$ Lep	UT 2009 Jan 10	-0.96	0.0	135.3	-105	114	117	26	0.11
$\gamma$ Lep	UT 2009 Jan 10	-0.96	90.0	135.3	-117	128	131	29	0.12
$\gamma$ Lep	UT 2009 Jan 10	-0.96	90.0	45.3	-99	108	111	25	0.09
$\gamma$ Lep	UT 2009 Jan 13	-1.25	0.0	134.8	-53	66	117	27	0.11
$\gamma$ Lep	UT 2009 Jan 13	-1.25	90.0	134.8	-58	72	128	30	0.12
$\gamma$ Lep	UT 2009 Jan 13	-1.25	90.0	44.8	-51	63	112	26	-0.02
$\gamma$ Oph	UT 2008 Jul 16	-1.09	0.0	131.3	382	98	81	4	0.35
$\gamma$ Oph	UT 2008 Jul 16	-1.09	90.0	131.3	410	104	86	4	0.35
$\gamma$ Oph	UT 2008 Jul 16	-1.09	90.0	41.3	374	96	79	3	0.23
$\gamma$ Oph	UT 2008 Jul 16	0.93	0.0	124.5	160	81	81	3	0.35
$\gamma$ Oph	UT 2008 Jul 16	0.93	90.0	124.5	218	109	110	4	0.35
$\gamma$ Oph	UT 2008 Jul 16	0.93	90.0	34.5	132	66	67	2	0.29
$\gamma$ Oph	UT 2008 Jul 16	2.18	0.0	115.4	211	43	82	3	0.35
$\gamma$ Oph	UT 2008 Jul 16	2.18	90.0	115.4	274	56	106	3	0.38
$\gamma$ Oph	UT 2008 Jul 16	2.18	90.0	25.4	184	38	71	2	0.29
$\gamma$ Oph	UT 2008 Jul 17	-1.20	0.0	131.5	21	119	81	4	0.35
$\gamma$ Oph	UT 2008 Jul 17	-1.20	90.0	131.5	22	126	85	4	0.35
$\gamma$ Oph	UT 2008 Jul 17	-1.20	90.0	41.5	20	117	79	3	0.23
$\gamma$ Oph	UT 2008 Jul 17	1.12	0.0	123.4	25	57	81	3	0.35
$\gamma$ Oph	UT 2008 Jul 17	1.12	90.0	123.4	33	77	110	4	0.35
$\gamma$ Oph	UT 2008 Jul 17	1.12	90.0	33.4	20	47	67	2	0.29
$\gamma$ Oph	UT 2008 Jul 17	2.20	0.0	115.2	246	54	82	3	0.35
$\gamma$ Oph	UT 2008 Jul 17	2.20	90.0	115.2	320	70	106	3	0.38

Table 4—Continued

Name	Date	HA	$i_{disk}$ ( $^{\circ}$ )	$PA_{disk}$ ( $^{\circ}$ )	$z_{ij}$	$\sigma_{ij}^{formal}$	$\sigma_j^{ext}$	$\sigma^*$	$R_{\text{half-light}}$ (AU)
$\gamma$ Oph	UT 2008 Jul 17	2.20	90.0	25.2	215	47	71	2	0.29
$\gamma$ Ser	UT 2008 Apr 16	0.73	0.0	123.6	-25	69	106	31	0.13
$\gamma$ Ser	UT 2008 Apr 16	0.73	90.0	123.6	-33	89	138	40	0.13
$\gamma$ Ser	UT 2008 Apr 16	0.73	90.0	33.6	-21	59	92	27	0.09
$\gamma$ Ser	UT 2008 Apr 16	1.46	0.0	118.7	227	86	107	30	0.13
$\gamma$ Ser	UT 2008 Apr 16	1.46	90.0	118.7	287	108	134	38	0.13
$\gamma$ Ser	UT 2008 Apr 16	1.46	90.0	28.7	203	77	95	27	0.09
$\gamma$ Ser	UT 2008 Apr 16	2.62	0.0	108.9	-81	108	107	27	0.13
$\gamma$ Ser	UT 2008 Apr 16	2.62	90.0	108.9	-98	130	129	33	0.13
$\gamma$ Ser	UT 2008 Apr 16	2.62	90.0	18.9	-75	100	99	25	-0.02
$\gamma$ Ser	UT 2008 Apr 17	2.40	0.0	110.9	-279	77	107	28	0.13
$\gamma$ Ser	UT 2008 Apr 17	2.40	90.0	110.9	-338	93	130	34	0.13
$\gamma$ Ser	UT 2008 Apr 17	2.40	90.0	20.9	-257	70	98	25	-0.02
$\gamma$ Ser	UT 2008 Apr 17	2.93	0.0	105.9	-366	102	107	27	0.13
$\gamma$ Ser	UT 2008 Apr 17	2.93	90.0	105.9	-435	122	128	32	0.13
$\gamma$ Ser	UT 2008 Apr 17	2.93	90.0	15.9	-340	95	100	25	-0.02
$\iota$ Peg	UT 2008 Jul 14	1.27	0.0	119.2	-167	53	105	25	0.14
$\iota$ Peg	UT 2008 Jul 14	1.27	90.0	119.2	-212	66	131	31	0.14
$\iota$ Peg	UT 2008 Jul 14	1.27	90.0	29.2	-147	46	92	21	-0.02
$\iota$ Peg	UT 2008 Jul 14	1.98	0.0	113.6	-159	55	105	24	0.14
$\iota$ Peg	UT 2008 Jul 14	1.98	90.0	113.6	-196	67	128	30	0.14
$\iota$ Peg	UT 2008 Jul 14	1.98	90.0	23.6	-143	49	94	22	-0.02
$\iota$ Per	UT 2009 Jan 11	1.34	0.0	119.8	-267	112	120	18	0.13
$\iota$ Per	UT 2009 Jan 11	1.34	90.0	119.8	-364	153	164	25	0.13
$\iota$ Per	UT 2009 Jan 11	1.34	90.0	29.8	-226	95	101	15	0.08
$\iota$ Psc	UT 2008 Aug 18	-0.46	0.0	129.8	-303	155	136	18	0.17
$\iota$ Psc	UT 2008 Aug 18	-0.46	90.0	129.8	-359	185	162	22	0.17
$\iota$ Psc	UT 2008 Aug 18	-0.46	90.0	39.8	-289	148	129	17	0.11
$\iota$ Psc	UT 2008 Oct 13	-1.79	0.0	131.9	80	106	136	18	0.17
$\iota$ Psc	UT 2008 Oct 13	-1.79	90.0	131.9	92	122	156	21	0.17
$\iota$ Psc	UT 2008 Oct 13	-1.79	90.0	41.9	77	103	132	18	0.11

Table 4—Continued

Name	Date	HA	$i_{disk}$ ( $^{\circ}$ )	$PA_{disk}$ ( $^{\circ}$ )	$z_{ij}$	$\sigma_{ij}^{formal}$	$\sigma_j^{ext}$	$\sigma^*$	$R_{half-light}$ (AU)
$\iota$ Psc	UT 2008 Oct 13	-0.93	0.0	131.0	90	138	135	19	0.17
$\iota$ Psc	UT 2008 Oct 13	-0.93	90.0	131.0	103	158	155	22	0.17
$\iota$ Psc	UT 2008 Oct 13	-0.93	90.0	41.0	88	134	132	18	0.11
$\kappa$ -1 Cet	UT 2009 Jan 10	-0.13	0.0	129.1	-107	158	129	21	0.09
$\kappa$ -1 Cet	UT 2009 Jan 10	-0.13	90.0	129.1	-145	213	174	28	0.09
$\kappa$ -1 Cet	UT 2009 Jan 10	-0.13	90.0	39.1	-101	148	121	19	0.07
KX Lib	UT 2008 May 26	1.25	0.0	132.7	527	214	260	105	0.07
KX Lib	UT 2008 May 26	1.25	90.0	132.7	871	350	425	174	0.07
KX Lib	UT 2008 May 26	1.25	90.0	42.7	480	195	237	96	0.06
KX Lib	UT 2008 May 26	2.14	0.0	127.0	191	309	270	80	0.08
KX Lib	UT 2008 May 26	2.14	90.0	127.0	338	544	476	141	0.08
KX Lib	UT 2008 May 26	2.14	90.0	37.0	171	278	243	72	0.06
$\lambda$ Aur	UT 2009 Jan 12	0.62	0.0	124.7	341	111	160	46	0.13
$\lambda$ Aur	UT 2009 Jan 12	0.62	90.0	124.7	487	158	227	66	0.13
$\lambda$ Aur	UT 2009 Jan 12	0.62	90.0	34.7	304	99	143	41	0.10
NSV 4765	UT 2009 Jan 10	1.90	0.0	114.7	-506	163	195	111	0.05
NSV 4765	UT 2009 Jan 10	1.90	90.0	114.7	-775	252	300	170	0.04
NSV 4765	UT 2009 Jan 10	1.90	90.0	24.7	-467	151	180	102	0.04
$\tau$ Boo	UT 2008 May 25	1.40	0.0	119.0	155	139	131	9	0.16
$\tau$ Boo	UT 2008 May 25	1.40	90.0	119.0	207	185	174	13	0.16
$\tau$ Boo	UT 2008 May 25	1.40	90.0	29.0	143	129	121	9	0.12
$\tau$ Boo	UT 2008 May 25	2.28	0.0	111.7	214	136	131	9	0.16
$\tau$ Boo	UT 2008 May 25	2.28	90.0	111.7	281	178	171	12	0.16
$\tau$ Boo	UT 2008 May 25	2.28	90.0	21.7	201	128	123	8	0.12
$\tau$ Boo	UT 2008 May 25	3.05	0.0	104.4	66	114	132	8	0.16
$\tau$ Boo	UT 2008 May 25	3.05	90.0	104.4	85	147	169	11	0.16
$\tau$ Boo	UT 2008 May 25	3.05	90.0	14.4	63	109	125	8	0.12
$\tau$ Boo	UT 2008 May 27	1.84	0.0	115.6	163	69	131	9	0.16
$\tau$ Boo	UT 2008 May 27	1.84	90.0	115.6	215	91	172	12	0.16
$\tau$ Boo	UT 2008 May 27	1.84	90.0	25.6	152	65	122	8	0.12
$\tau$ Boo	UT 2008 May 27	2.76	0.0	107.3	122	97	132	9	0.16



Table 4—Continued

Name	Date	HA	$i_{disk}$ ( $^{\circ}$ )	$PA_{disk}$ ( $^{\circ}$ )	$z_{ij}$	$\sigma_{ij}^{formal}$	$\sigma_j^{ext}$	$\sigma^*$	$R_{\text{half-light}}$ (AU)
$\tau$ Boo	UT 2008 May 27	2.76	90.0	107.3	158	126	170	11	0.16
$\tau$ Boo	UT 2008 May 27	2.76	90.0	17.3	115	92	124	8	0.12
$\theta$ Per	UT 2009 Jan 11	0.49	0.0	127.3	400	62	111	21	0.13
$\theta$ Per	UT 2009 Jan 11	0.49	90.0	127.3	544	84	150	29	0.13
$\theta$ Per	UT 2009 Jan 11	0.49	90.0	37.3	352	55	98	19	0.09
$\theta$ Per	UT 2009 Jan 11	2.32	0.0	110.6	-321	107	111	22	-0.02
$\theta$ Per	UT 2009 Jan 11	2.32	90.0	110.6	-436	146	151	31	0.11
$\theta$ Per	UT 2009 Jan 11	2.32	90.0	20.6	-276	92	95	19	0.09
$\theta$ Per	UT 2009 Jan 12	1.93	0.0	114.3	-82	65	111	22	0.13
$\theta$ Per	UT 2009 Jan 12	1.93	90.0	114.3	-113	90	152	31	0.11
$\theta$ Per	UT 2009 Jan 12	1.93	90.0	24.3	-70	56	95	19	0.09
$\nu$ And	UT 2008 Nov 12	2.53	0.0	108.3	-300	128	123	20	0.13
$\nu$ And	UT 2008 Nov 12	2.53	90.0	108.3	-394	169	162	27	0.13
$\nu$ And	UT 2008 Nov 12	2.53	90.0	18.3	-263	113	108	18	0.11
$\nu$ And	UT 2008 Nov 12	3.43	0.0	99.7	40	87	123	21	0.13
$\nu$ And	UT 2008 Nov 12	3.43	90.0	99.7	50	110	156	26	0.13
$\nu$ And	UT 2008 Nov 12	3.43	90.0	9.7	36	79	111	18	0.11

Note. — Table 4 is published in its entirety in the electronic edition of the *Astrophysical Journal*. A portion is shown here for guidance regarding its form and content.

Table 5. Average number of zodis for each target.

Name	$z \pm \sigma_z$	$\chi = \frac{z}{\sigma_z}$	$3\sigma$ Upper limits
Detections:			
$\eta$ Crv	$1246 \pm 257$	4.8	...
Possible detections:			
$\gamma$ Oph	$198 \pm 77$	2.6	429
$\alpha$ Aql	$573 \pm 191$	3.0	1146
Non-detections:			
107 Psc	$107 \pm 192$	0.6	683
1 Ori	$43 \pm 48$	0.9	187
47 UMa	$67 \pm 187$	0.4	628
61 Cyg A	$143 \pm 194$	0.7	725
70 Oph	$67 \pm 159$	0.4	544
HIP 54035	$-227 \pm 179$	-1.3	537
$\beta$ Com	$237 \pm 245$	1.0	972
$\beta$ Vir	$-9 \pm 214$	-0.0	642
$\chi$ -1 Ori	$-60 \pm 128$	-0.5	384
$\delta$ Tri	$-380 \pm 191$	-2.0	573
$\gamma$ Lep	$-80 \pm 84$	-1.0	252
$\gamma$ Ser	$-171 \pm 89$	-1.9	267
$\iota$ Peg	$-169 \pm 111$	-1.5	333
$\iota$ Per	$-281 \pm 139$	-2.0	417
$\iota$ Psc	$-84 \pm 106$	-0.8	318
$\kappa$ -1 Cet	$-115 \pm 172$	-0.7	516
KX Lib	$469 \pm 341$	1.4	1492
$\lambda$ Aur	$368 \pm 190$	1.9	938
NSV 4765	$-564 \pm 262$	-2.2	786
$\tau$ Boo	$151 \pm 101$	1.5	454
$\theta$ Per	$-54 \pm 111$	-0.5	333
$\nu$ And	$-72 \pm 166$	-0.4	498
Average:			567



Table 6. Spitzer/IRS – KIN comparison.

Name	HD	Spitzer/IRS <sup>a</sup>		KIN
		$\frac{F_{dust}}{F_{\star}}$	$z$ <sup>b</sup> ( $3\sigma$ limit)	$z$ ( $3\sigma$ limit)
47 Uma	95128	$-0.022 \pm 0.013$	1110	628
$\beta$ Com	114719	$0.014 \pm 0.01$	830	972
$\gamma$ Lep	38393	$0.001 \pm 0.01$	750	252
$\iota$ Psc	2223658	$-0.007 \pm 0.014$	970	318
kx Lib	131977	$0.002 \pm 0.01$	1600	1492
$\tau$ Boo	120136	$0.011 \pm 0.014$	970	454
$\theta$ Per	16895	$0.003 \pm 0.01$	750	333
$\nu$ And	9826	$-0.003 \pm 0.01$	970	498

<sup>a</sup>from Beichman et al. (2006a) and Lawler et al. (2009).

<sup>b</sup>computed as:  $L_{dust}/L_{\star} \times 10^{-7}$ .